ACS APPLIED MATERIALS & INTERFACES

Research Article

www.acsami.org

Polypropylene/Polyaniline Nanofiber/Reduced Graphene Oxide Nanocomposite with Enhanced Electrical, Dielectric, and Ferroelectric Properties for a High Energy Density Capacitor

Sunghun Cho,[†,‡] Minkyu Kim,[‡] Jun Seop Lee,[‡,§] and Jyongsik Jang*[,‡]

[†]Department of Chemistry and Biochemistry, University of California, Los Angeles (UCLA), Los Angeles, California 90095, United States

[‡]Program of Chemical Convergence for Energy and Environment (C2E2), School of Chemical and Biological Engineering, College of Engineering, Seoul National University, Shinlimdong 56-1, Seoul 151-742, Korea

[§]Electrochemical Energy Laboratory & Materials Science and Engineering Program, The University of Texas at Austin, Austin, Texas 78712, United States

Supporting Information

ABSTRACT: This work demonstrates a ternary nanocomposite system, composed of polypropylene (PP), redoped PANI (r-PANI) nanofibers, and reduced graphene oxides (RGOs), for use in a high energy density capacitor. r-PANI nanofibers were fabricated by the combination methods of chemical oxidation polymerization and secondary doping processes, resulting in higher conductivity ($\sigma \approx 156$ S cm^{-1}) than that of the primarily doped PANI nanofibers ($\sigma \approx 16$ S cm^{-1}). RGO sheets with high electron mobility and thermal stability can enhance the conductivity of r-PANI/RGO ($\sigma \approx 220$ S cm^{-1}) and thermal stability of PP matrix. These findings could be extended to combine the advantages of r-PANI nanofibers and RGO sheets for developing an efficient means of preparing PP/r-PANI/RGO nanocomposite. When the r-PANI/RGO cofillers (10 vol %) were added to PP matrix, the resulting PP/r-PANI/RGO nanocomposite exhibited high dielectric constant ($\varepsilon' \approx 51.8$) with small dielectric loss ($\varepsilon'' \approx 9.3 \times 10^{-3}$). Furthermore, the PP/r-PANI/RGO nanocomposite was used for an energy-harvesting device, which demonstrated high energy density ($U_e \approx 12.6$ J cm^{-3}) and breakdown strength ($E \approx 5.86 \times 10^3$ kV cm^{-1}).

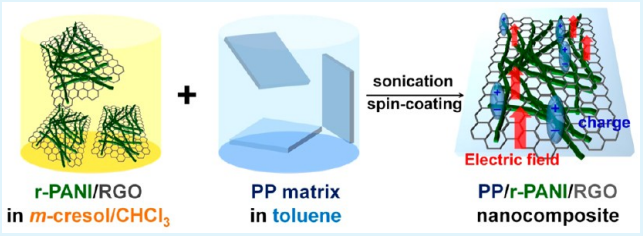

KEYWORDS: *polypropylene, polyaniline, graphene, nanocomposite, dielectric capacitor*

INTRODUCTION

With the development of capacitor technology, there have been great advancements in dielectric materials with high energy density.[1−24] In particular, polymer materials, such as polyvinylidene fluoride (PVDF),[1−7] polypropylene (PP),[8−12] polyimide (PI),[13] and polyphenylene sulfide (PPS),[14] have attracted interest due to their intrinsic advantages, such as high breakdown strength, facile processability, low dielectric loss, and lightness. Among the polymeric materials, PP is one of the attractive candidates for dielectric capacitors, since the PP provides a higher breakdown electric field and lower dielectric loss than the other polymer matrices.[8−12] Recently, Chung et. al reported that the dielectric and ferroelectric properties of PP could be significantly intensified via functionalization of the PP surface.[9,12] However, the PP still suffers from a low dielectric constant ($\varepsilon' \approx 2.2$) and small energy density ($U_e \approx 1.2$ J cm^{-3}), which limits its practical applicability in energy harvesters.[10−12] Thus, the polymeric thin films having high dielectric permittivity are highly desired.

Recently, polymer nanocomposites filled with a variety of fillers, such as ceramics, metals, carbons, and conducting polymers, have attracted great attention because of their synergistic effects from the high dielectric permittivity of the fillers and the high breakdown electric field of the polymer matrices.[4−12,14,16] In particular, the inorganic fillers, including $BaTiO_3$,[4−7,15] $SrTiO_3$,[16−18] $Pb(Zr_xTi_{1-x})O_3-PbTiO_3$,[19] $AlTiO_3$,[20,21] Al_2O_3,[10,11,22] ZrO_2,[10,23] MgO,[10,11] and their mixtures,[10,11,19,24] have been extensively used as dielectric capacitors owing to their high dielectric permittivity of several hundreds. Marks et al. reported that the $BaTiO_3-$ and $ZrO_2-Al_2O_3$ nanoparticles can significantly improve the dielectric permittivity and energy density of the PP nanocomposites.[10,11] Despite such improvements, these polymer−inorganic nanocomposites require a high filler content to improve their dielectric properties, and the increased filler content of the inorganic materials usually deteriorates the flexibility and breakdown strength of the polymer matrices.[4−24] Considering these facts, more appropriate fillers with eco-friendliness, high flexibility, and low filler loading are needed for the construction of the high-performance PP-based capacitors.

Received: June 19, 2015
Accepted: September 23, 2015
Published: October 2, 2015

DOI: 10.1021/acsami.5b05467
ACS Appl. Mater. Interfaces 2015, 7, 22301−22314

Scheme 1. (a) Overall Procedures for Fabricating (a) r-PANI Nanofibers, (b) RGO Sheets, and (c) PP/r-PANI/RGO Nanocomposite

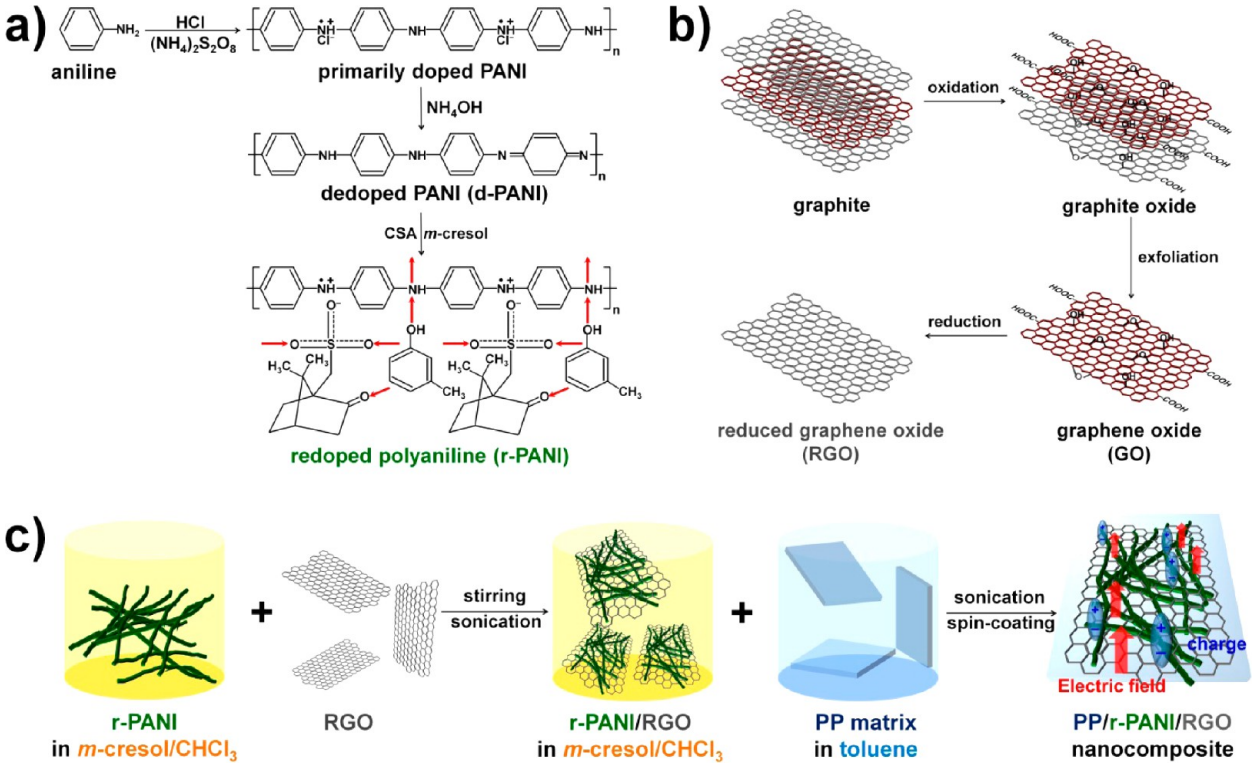

Polyaniline (PANI) is one of the most promising candidates for dielectric materials due to its fascinating virtues, such as facile synthesis, reversible redox behavior, good electrical conductivity, and high dielectric permittivity ($\varepsilon' \approx 10^2$–$10^3$).[25,26] Moreover, the PANI of nanometer sizes (<100 nm) provide larger surface areas and smaller dimensions compared with their bulky counterparts, which permit enhanced interactions with the surrounding polymer matrices.[27−29] In particular, there have been significant improvements in the conductivity of PANI nanomaterials via a secondary doping method.[30−32] These advantages of PANI nanomaterials make it suitable for conducting fillers in the PP matrix. Therefore, there has been extensive work on the PP−PANI binary nanocomposites.[33−37] However, the higher filler loading of the PANI can also cause higher dielectric losses and leakage current, which limits the application of PP−PANI nanocomposites as dielectric materials.[25,26] To solve these problems, PANI has been frequently combined with carbon nanomaterials, such as graphene[38,39] and carbon nanotubes (CNT),[40−42] to improve its charge transfer ability and thermal and mechanical properties.

Graphene, a one-atom-thick planar structure of sp^2-bonded carbon, is one of the most attractive fillers for various polymer matrices due to its outstanding electron mobility, thermal stability, mechanical strength, and flexibility.[43−48] More importantly, the charge transport properties of the PANI can be significantly intensified through the face-to-face interactions with the graphene sheets, and this finding has been extended to the combination of PANI nanomaterials and graphene sheets for various applications, such as capacitors,[32] sensors,[49,50] antenna,[51,52] and solar cells.[53] Nevertheless, the synergistic effects from the PANI nanomaterials and graphene-based materials on the dielectric and ferroelectric properties of the PP have seldom been reported. Accordingly, the development of high-performance PP/PANI/graphene nanocomposites with high dielectric constant, low dielectric loss, and large energy density is still a challenge.

Herein, we report the fabrication of polypropylene/redoped polyaniline/reduced graphene oxide (PP/r-PANI/RGO) ternary nanocomposite for high-energy density capacitor. In these nanocomposite films, r-PANI nanofibers and RGO sheets acted as cofillers to enhance dielectric permittivity, electrical conductivity, and ferroelectric performance of the PP-based nanocomposite. The r-PANI nanofibers that are prepared by combining the oxidation polymerization and secondary doping methods demonstrated about 10 times higher electrical conductivity ($\sigma \approx 156$ S cm^{-1}) than that of the PANI ($\sigma \approx 16$ S cm^{-1}). RGO sheets were highly dispersible with r-PANI nanocomposite, resulting in the improved conductivity of r-PANI/RGO ($\sigma \approx 220$ S cm^{-1}); this improvement in the conductivity of r-PANI/RGO accounts for the enhanced protonation levels and longer conjugation lengths than those of the PANI and r-PANI nanofibers. Although the r-PANI/RGO cofiller did not affect the crystalline of PP matrix, the cofiller consequently improved the melting (T_m) and crystalline temperature (T_c) of PP nanocomposite. As a result of combination of these three components (PP, r-PANI nanofiber, and RGO sheet), the PP/r-PANI/RGO nanocomposite exhibited improved dielectric permittivity ($\varepsilon' \approx 51.8$), comparable dielectric loss ($\varepsilon'' \approx 9.3 \times 10^{-3}$), and enhanced energy density ($U_e \approx 12.6$ J cm^{-3}) compared with that of the pristine PP ($\varepsilon' \approx 2.3$, $\varepsilon'' \approx 4.9 \times 10^{-4}$, and $U_e \approx 0.58$ J cm^{-3}).

RESULTS AND DISCUSSION

Fabrication and Characterization of PP/r-PANI/RGO Nanocomposite. The overall procedure for fabricating

DOI: 10.1021/acsami.5b05467
ACS Appl. Mater. Interfaces 2015, 7, 22301−22314

polypropylene/redoped polyaniline/reduced graphene oxide (PP/r-PANI/RGO) nanocomposite, which is based on chemical oxidation polymerization and secondary doping methods, is demonstrated in Scheme 1. Scheme 1a represents the fabrication procedure of r-PANI nanofibers. In the first step, aniline monomers were protonated using hydrochloric acid (HCl) and subsequently reacted with ammonium persulfate (APS) to produce the PANI nanofibers. For secondary doping of the PANI nanofibers, as-prepared PANI nanofibers were deprotonated using ammonia (NH_4OH) solution; the dedoped PANI (d-PANI) nanofibers have been redoped with camphorsulfonic acid (CSA) in aqueous solution. The secondarily doped PANI structures are highly compatible with the mixture of *m*-cresol/chloroform for the following reasons. (1) Sulfonic acid ($-SO_3H$) of CSA can form strong hydrogen-bonding interactions with the hydroxyl group ($-OH$) of *m*-cresol. (2) These hydrogen-bonding forces induce more electrostatic repulsion interactions between the positive charges on the PANI structures, which consequently expand the coil conformation of PANI chains. (3) The covalent methyl group of *m*-cresol interacts with the $CHCl_3$. For these reasons, the mixture of *m*-cresol/$CHCl_3$ was selected as a cosolvent for increasing the conductivity of r-PANI.[30−32] RGO sheets have been prepared according to the modified Hummers method (Scheme 1b).[43,44] In the first step, GO sheets were obtained by simple oxidation of graphite, and the GO sheets were redispersed in the *m*-cresol solvent. The GO sheets dispersed in the *m*-cresol solvent were reduced with hydrazine (N_2H_4). As-prepared RGO sheets were redispersed in the *m*-cresol; then the RGO solution was inserted into the r-PANI solution via vigorous stirring and sonochemical treatment. The r-PANI/RGO cofillers dissolved in the *m*-cresol/$CHCl_3$ cosolvent have been mixed with PP matrix dissolved in toluene (Scheme 1c). According to Hansen's equation, toluene has very similar dispersion (δ_d), hydrogen-bonding (δ_h), and polarity interaction (δ_p) parameters compared with that of *m*-cresol (Table S1).[54] Accordingly, the PANI/RGO cofiller dissolved in *m*-cresol could be dispersible with the toluene. The ternary PP/r-PANI/RGO was formed as films on the glass substrate using the spin-coating method; the fabricated films had a thickness of 40 μm.

Figure 1 shows transmission electron microscopy (TEM) images of PANI, r-PANI, RGO, and PP/r-PANI/RGO nanocomposite. PANI nanofibers were synthesized by the combination methods of chemical oxidation polymerization and secondary doping, and their diameters and lengths were 40−60 nm and 0.6−1.5 μm, respectively (Figure 1a). RGO sheets were prepared using a Hummers method, and their sizes ranged from 0.7 to 1.7 μm (Figure 1b). These r-PANI nanofibers and RGO sheets were dispersed in the PP matrix, demonstrating that the r-PANI/RGO cofillers could be successfully introduced into the PP matrix dissolved in the mixture of *m*-cresol/$CHCl_3$/toluene (Figure 1c).

To observe the effects of r-PANI and RGO sheets on the spherulite growth of PP nanocomposites, polarized optical microscopy (POM) images of the PP nanocomposites are shown in Figure 2a−e. After the addition of fillers to the PP matrices, the sizes of spherulites decreased as follows: PP/PANI < PP/r-PANI < PP/r-PANI/RGO < PP/RGO < pristine PP. The results indicate that the PANI nanofibers acted as nuclei, resulting in the formation of smaller and imperfect spherulites than that of the PP/RGO.[55−59] Nevertheless, the PP/r-PANI/RGO showed more spherulites in a limited space than those of the pristine PP and PP/RGO, indicating that both the r-PANI and the RGO acted as multiple nuclei. The spherulite growth rate of the PP nanocomposites was in good agreement with the POM images (Figure 2f). These results can

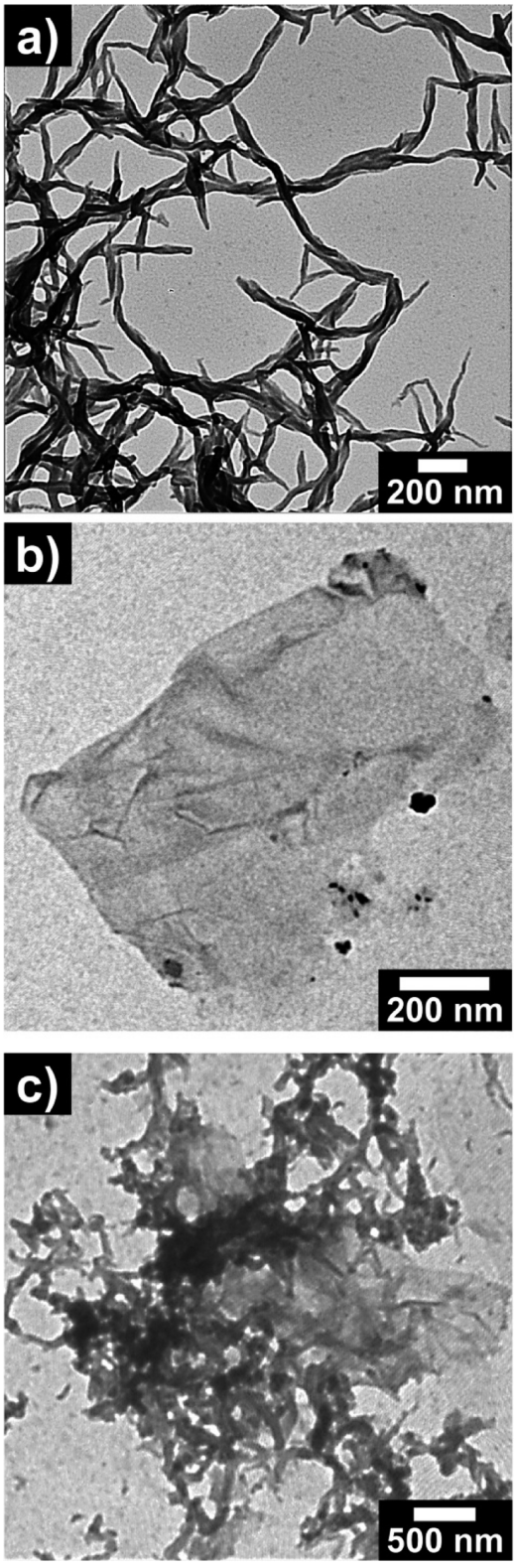

Figure 1. TEM images of (a) r-PANI nanofiber, (b) RGO sheet, and (c) PP/r-PANI/RGO (90:5:5, v/v/v) nanocomposite. The concentration of fillers in PP/r-PANI/RGO is 10 vol % with respect to PP nanocomposite.

DOI: 10.1021/acsami.5b05467
ACS Appl. Mater. Interfaces 2015, 7, 22301−22314

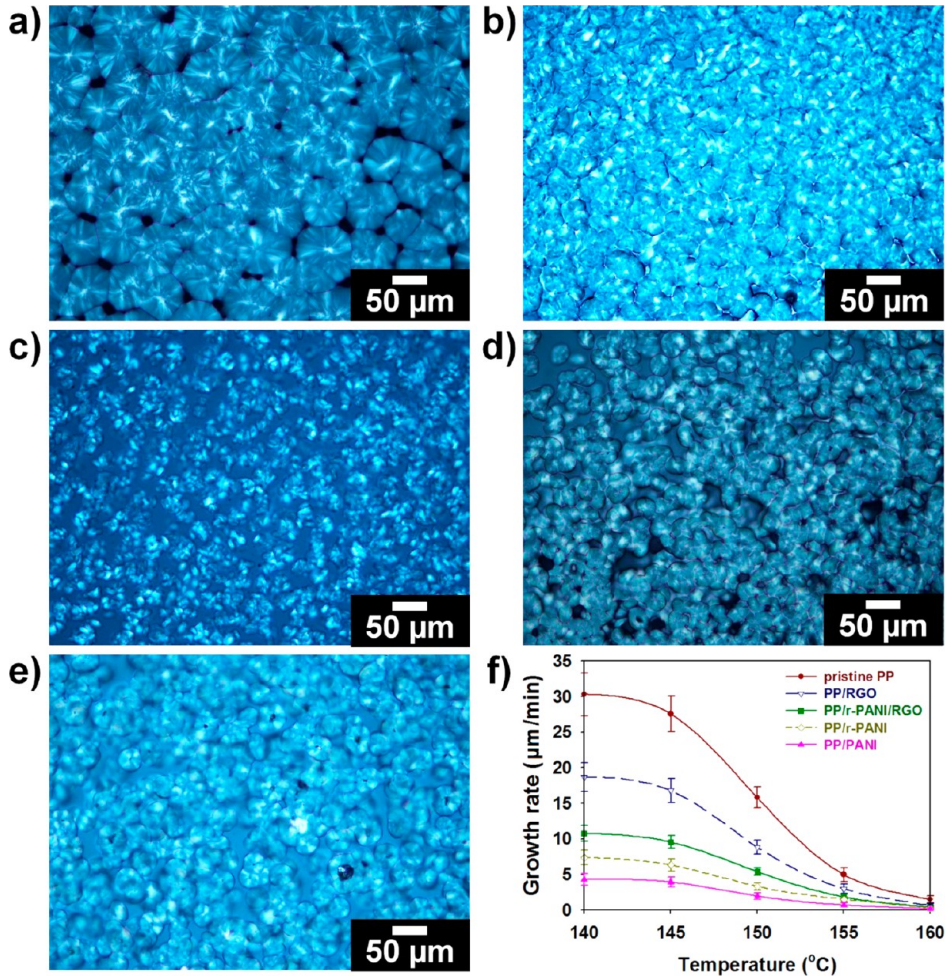

Figure 2. POM images of PP nanocomposites containing different fillers after isothermal crystallization at 160 °C: (a) pristine PP, (b) RGO, (c) PANI, (d) r-PANI, and (e) r-PANI/RGO. (f) Spherulite growth rate of nanocomposites containing different fillers after isothermal crystallization at 160 °C for 10 min. The concentration of all fillers is 10 vol % with respect to PP nanocomposites.

be explained by the following points. (1) Movements of the PP chains are more effectively restricted by PANI nanofibers than those of the RGO sheets. (2) Thus, the end-to-end distance of PP chains decreases with decreasing interparticle distance between the fillers. (3) PANI nanofibers induce a larger activation energy for crystallizing PP compared with that of the RGO sheets, which lowers the spherulite growth rate.[55−59]

To monitor the effects of secondary doping and the presence of RGO sheets on the crystalline structure of PANI, X-ray diffraction (XRD) patterns of the reduced graphene oxide (RGO), polyaniline (PANI), dedoped polyaniline (d-PANI), redoped polyaniline (r-PANI), and r-PANI/RGO are shown in Figure 3a. A broad diffraction peak appeared at 2θ = 24.6° (3.62 Å) in the spectrum of RGO, which is close that of natural graphite with an interlayer distance of 3.39 Å.[32,50] In the spectrum of PANI nanofibers, three distinctive peaks for PANI appeared at 2θ = 15.1°, 20.4°, and 25.6°, which correspond to (011), (020), and (200) planes of PANI, respectively.[30−32,50] After the reduction of PANI nanofibers, the peak at 2θ = 25.6° was reduced, whereas the peaks at 2θ = 15.1° and 20.4° became stronger compared with that of the PANI. The changes in the XRD pattern of d-PANI may be due to the deprotonation of PANI from the protonated emeraldine salt (ES) to the deprotonated emeraldine base (EB).[30−32] After the d-PANI was redoped by CSA, the diffraction peak for the (200) plane in the pattern of r-PANI significantly increased compared with those of the PANI and d-PANI. After combining the r-PANI nanofibers with the RGO sheets, the characteristic peaks for PANI were clearly observed, while the broad peak of RGO could not be distinguished. This indicates that the RGO sheets were highly intercalated with the PANI nanofibers.[32,50] The relative ratio of the peak intensities for (011), (020), and (200) was estimated using the equation $(I_{200})/(I_{011} + I_{020} + I_{200})$, where I_{011}, I_{020}, and I_{200} denote the peak intensities for the (011), (020), and (200) planes, respectively. The relative proportion of I_{200} in the XRD patterns increased as follows: d-PANI (0.32) < PANI (0.60) < r-PANI (0.71) < r-PANI/RGO (0.74). According to previous work, the diffraction peak for the (200) plane is related to the conjugation length for delocalizing electrons in the π-conjugated PANI. It was evident that the proportion of I_{200} increased after the addition of RGO sheets into the secondarily doped r-PANI. The increased proportion of I_{200} in the XRD pattern of r-PANI/RGO may be owing to the following reasons. (1) The secondary doping of PANI induces the expanded coil conformation and higher linearity of the PANI chains. (2) The RGO sheets with high electron mobility further enhance the face-to-face interactions in the PANI structure, which subsequently result in the extended conjugation lengths of the PANI structure.[30−32,39,50]

DOI: 10.1021/acsami.5b05467
ACS Appl. Mater. Interfaces 2015, 7, 22301−22314

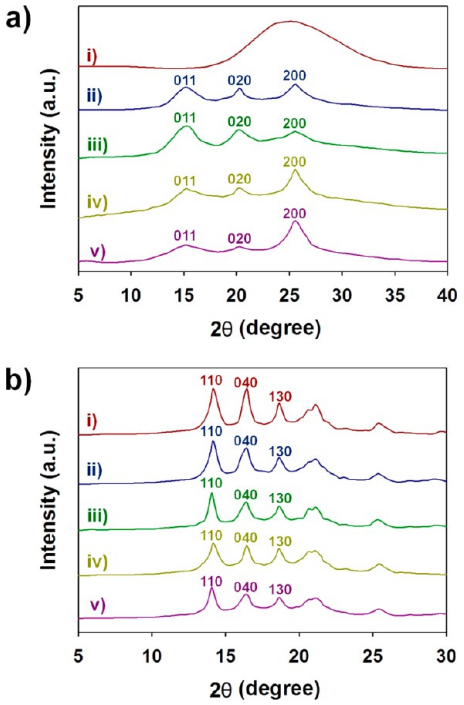

Figure 3. (a) XRD patterns of RGO (red), PANI (blue), d-PANI (green), r-PANI (olive green), and r-PANI/RGO (purple). (b) XRD patterns of pristine PP (red), PP nanocomposites filled with PANI (blue), d-PANI (green), r-PANI (olive green), and r-PANI/RGO (purple). The concentration of all fillers is 10 vol % with respect to PP nanocomposites.

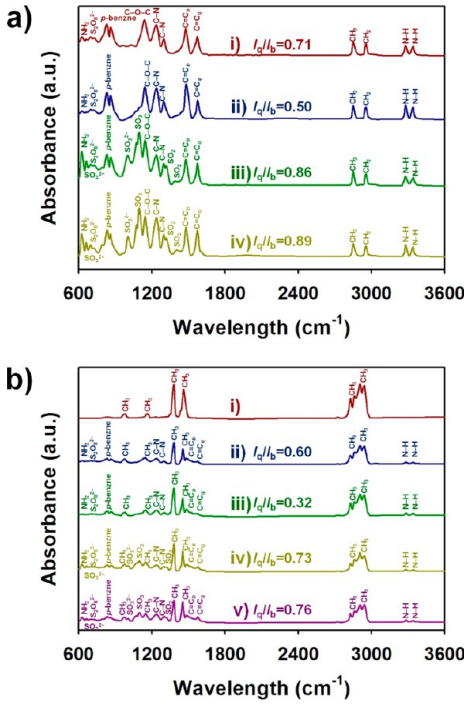

Figure 4. (a) FT-IR spectra of PANI (red), d-PANI (blue), r-PANI (green), and r-PANI/RGO (olive green). (b) FT-IR spectra of pristine PP (red), PP nanocomposites filled with PANI (blue), d-PANI (green), r-PANI (olive green), and r-PANI/RGO (purple). The concentration of all fillers is 10 vol % with respect to PP nanocomposites.

To further confirm the crystalline type of the PP nanocomposites filled with different fillers, the XRD spectra of the pristine PP, PP/PANI, PP/PANI/RGO, PP/d-PANI/RGO, and PP/r-PANI/RGO are shown in Figure 3b. In the XRD spectrum for pristine PP, the peaks appeared at 2θ = 14.2°, 16.8°, and 18.7°, corresponding to the (110), (040), and (130) planes of α-form PP, respectively.[57,59] In the XRD spectra of PP nanocomposites filled with PANI nanofibers, RGO sheets, and r-PANI/RGO cofillers, no characteristic peaks for PANI and RGO were found except the diffraction peaks of the α-form PP. This suggests that the PANI nanofibers and RGO sheets were well dispersed in the PP matrix, and these two fillers did not affect the crystalline structure of the PP.

To investigate the changes in the chemical bonding properties of different fillers, FT-IR spectra of the RGO, PANI, d-PANI, r-PANI, and r-PANI/RGO cofiller are shown in Figure 4a. Characteristic peaks for the oxygenated functional groups of GO appeared at 1043 (C−OH stretching), 1221 (C−O−C stretching), 1382 (C−O stretching), 1618 (C═C stretching), and 3441 cm^{-1} (O−H stretching), and these peaks were reduced with increasing reduction time (Figure S1, Table S2).[60] The results suggest that the hydrogen bonding of RGO sheets may decrease with increasing reduction degree of GO. In the FT-IR spectrum of PANI nanofibers, distinctive bands were observed at 625 (NH_2 deformation of aromatic amine), 833, 862 (out of plane bending for para-substituted benzene ring), 1145 (C−O−C stretching), 1236 (C−N stretching of benzenoid amine), 1295 (C−N stretching of aromatic amine), 1480 (C═C stretching of benzenoid unit), 1556 (N−H deformation of secondary amine), 1575 (C═C stretching of quinoid unit), 2851 (CH_2 symmetric stretching), 2956 (CH_2 asymmetric stretching), 3280, and 3340 cm^{-1} (N−H stretching of secondary amine) (Table S3).[29,31,32,44,60] The bands at 698 and 730 cm^{-1} in the spectrum of PANI nanofibers are attributable to the $S_2O_8^{2-}$ of APS. To determine the effects of the secondary doping process and RGO on the doping level of PANI, the relative ratios of the peak intensities for C═C stretching of quinoid and benzenoid units were calculated using the equation I_q/I_b, where I_q and I_b denote the peak intensities for C═C stretching of quinoid and benzenoid units, respectively. After the reduction of PANI nanofibers with NH_4OH, the peak for the C═C stretching vibration mode of the quinoid unit (1575 cm^{-1}) decreased as represented in the FT-IR spectrum of d-PANI. This implies changes in the PANI structure from the protonated ES to the deprotonated EB.[29,32] When the d-PANI was redoped with CSA, the peaks at 662, 1005 (SO_3^{2-} of CSA), 1083, and 1098 cm^{-1} (symmetric SO_3 stretching) became distinctive as shown in the FT-IR spectrum of r-PANI. In addition, the peak intensity for the C═C stretching of the quinoid unit became stronger than those of the PANI (I_q/I_b = 0.50) and d-PANI (I_q/I_b = 0.71). Moreover, the r-PANI/RGO cofiller showed a higher I_q/I_b (0.89) ratio compared with the r-PANI (I_q/I_b = 0.86). These results are attributable to the following points. (1) RGO sheets may enhance face-to-face stacking interactions between PANI chains, which extend the π-conjugated structure of PANI. (2) Due to the elongated conjugation length, r-PANI/RGO cofiller may permit better transport of charge carriers compared to those of the PANI and r-PANI. (3) Consequently, the enhanced charge carrier transport of r-PANI/RGO cofiller facilitates the protonation of PANI from a reduced structure (benzenoid unit) to an oxidized structure (quinoid unit).[29,31,32,44]

DOI: 10.1021/acsami.5b05467
ACS Appl. Mater. Interfaces 2015, 7, 22301−22314

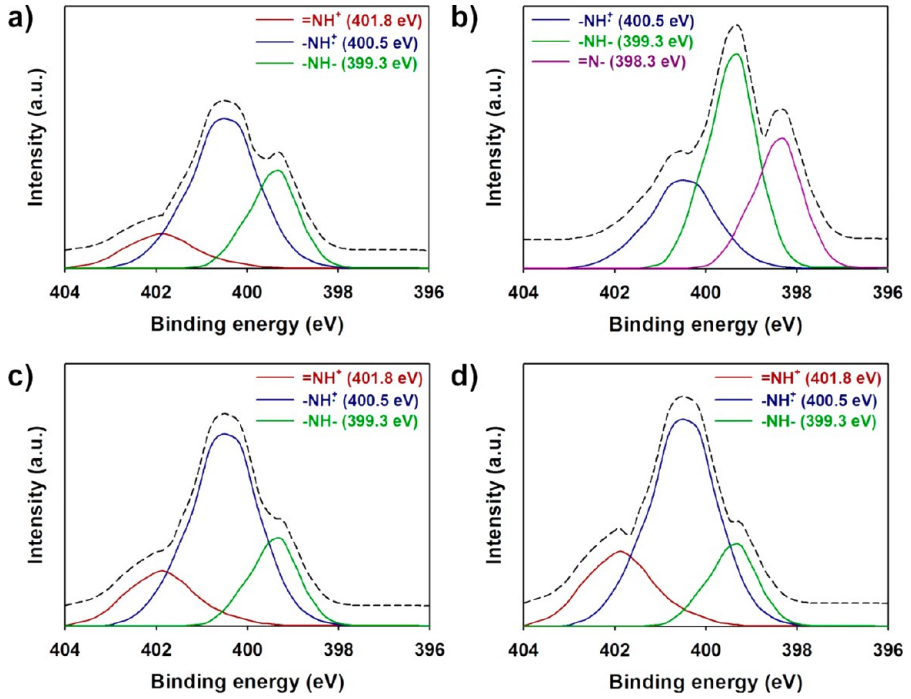

Figure 5. XPS core spectra in the N(1s) region of (a) PANI, (b) d-PANI, (c) r-PANI, and (d) r-PANI/RGO.

To represent the effects of r-PANI/RGO cofillers on the chemical structure of PP nanocomposites, FT-IR spectra of pristine PP and PP nanocomposites filled with RGO, PANI, r-PANI, and r-PANI/RGO cofiller are shown in Figure 4b. Characteristic peaks for the PP were observed at 957 (CH_3 rocking), 1148 (CH_3 wagging), 1398 (CH_3 symmetric deformation), 1459 (CH_3 asymmetric deformation), 2825, 2857 (CH_3 symmetric stretching), 2905, and 2937 cm^{-1} (CH_3 asymmetric stretching) (Table S4).[34,60] In the spectra of PP nanocomposites, the peaks for C=C stretching of the benzenoid and quinoid units appeared at 1483 and 1576 cm^{-1}, respectively. No peaks for RGO were found in the spectrum of PP/RGO, suggesting that the RGO sheets may be highly intercalated between the PP chains. The I_q/I_b ratio of PP nanocomposites increased as follows: PP/PANI (0.67) < PP/r-PANI (0.73) < PP/r-PANI/RGO (0.76). The results are consistent with the tendency shown in Figure 4a. These results indicate that the protonation levels of fillers in the PP matrix were well retained, which may affect the electrical properties of the PP nanocomposites.

X-ray photon spectroscopy (XPS) was used to monitor the binding energies that reflect the elemental compositions and protonation states of the samples (Figures 5 and S2). Figure 5a–d represents the N(1s) core spectra of the PANI, r-PANI, and r-PANI/RGO. The protonated PANI nanofibers showed three peaks at 399.3, 400.5, and 401.8 eV, corresponding to −NH− (benzenoid amine), − $NH^{\bullet+}$ (radical cation), and =NH^+ (imine cation), respectively.[29,32,50] In the N 1s spectrum of d-PANI, the peak for =NH^+ disappeared while the peak for −N= (imine nitrogen) newly appeared. This suggests that the PANI nanofibers were successfully deprotonated with NH_4OH.[29,32] The peak for −N= disappeared after redoping the d-PANI with CSA, indicating that the CSA not only dopes the −NH− but also dopes the −N= in the PANI.[29] To estimate the protonation states of samples, the ratio of N^+ species (sum of $-NH^{\bullet+}$ and =NH^+) to N species (sum of −N=, −NH−, −NH−, $-NH^{\bullet+}$, and =NH^+) was calculated. This ratio was 0.65, 0.74, and 0.78 for the PANI, r-PANI, and r-PANI/RGO, respectively (Table 1). The N^+/N ratio was in good agreement with the results of XRD and FT-IR, indicating that the secondary doping of PANI and the presence of RGO sheets increase the protonation level of PANI (Table 2).[29,32,50] Figure S2 shows fully scanned XPS patterns of PANI, r-PANI, RGO, and r-PANI/RGO. A weak peak for N(1s) was found in the spectrum of RGO, indicating that the GO sheets were appropriately reduced with hydrazine (N_2H_4).[32,43,44,50] The PANI exhibited five peaks located at 164, 231, 285, 400, and 532 eV corresponding to S(2p), S(2s), C(1s), N(1s), and

Table 1. Peak Analyses of XPS Core Spectra in the N(1s) region of PANI, d-PANI, r-PANI, and r-PANI/RGO

	XPS atomic ratio				
samples	−N=	−NH−	$-NH^{\bullet+}$	=NH^+	N^+/N ratio[a]
PANI		0.12	0.53	0.35	0.65
d-PANI	0.20	0.51	0.29		0.20
r-PANI		0.16	0.57	0.26	0.74
r-PANI/RGO		0.21	0.57	0.23	0.78

[a]Values were calculated using the N 1s core spectra of the samples.

Table 2. Protonation Level of Different Fillers Obtained from the FT-IR, XRD, and XPS Measurements

sample	XRD[a]	FT-IR[b]	XPS[c]
PANI	0.60	0.71	0.65
d-PANI	0.32	0.50	0.20
r-PANI	0.71	0.86	0.74
r-PANI/RGO	0.74	0.89	0.78

[a]Value was estimated from the peak intensity ratio of the (200) plane to the (011) and (020) planes. [b]Value was estimated from the peak intensity ratio of the quinoid unit to the benzenoid unit. [c]Value was estimated from the peak intensity ratio of N^+ species to N species.

DOI: 10.1021/acsami.5b05467
ACS Appl. Mater. Interfaces 2015, 7, 22301−22314

O(1s), respectively.[29,32,50] The C content in the r-PANI/RGO cofiller became higher compared with that of the r-PANI because of the presence of RGO (Table S5).[50]

Differential scanning calorimetry (DSC) thermographs of PP nanocomposites filled with the d-PANI, PANI, r-PANI, and r-PANI/RGO cofiller are shown in Figure 6a. There were no

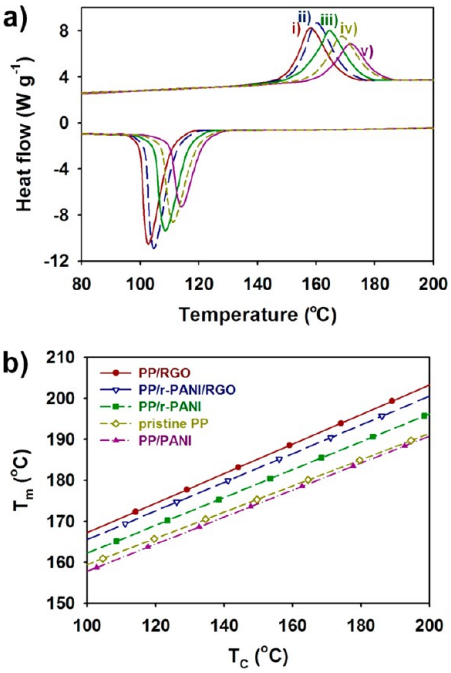

Figure 6. (a) DSC thermographs of PP nanocomposites filled with PANI (red), pristine PP (blue), r-PANI (green), r-PANI/RGO (olive green), and RGO (purple). (b) Hoffman–Weeks plots for PP nanocomposites filled with different fillers. The concentration of all fillers is 10 vol % with respect to PP nanocomposites.

multiple peaks in the thermographs, indicating that the fillers do not significantly change the crystalline structure of PP from monoclinic α-PP to hexagonal β-PP.[37,56] The degree of crystallinity (X_c) for PP nanocomposites was calculated using the equation $X_c = \Delta H_m/(\Delta H_\alpha \times w_{PP}) \times 100\%$, where ΔH_m and ΔH_α denote the heat fusions of samples and 100% crystalline α-PP (209 J g^{-1}), respectively, and w_{pp} refers to the weight fraction of PP matrix in the samples. X_c was reduced after the addition of fillers to the PP matrix, implying that the fillers induce imperfect crystals in the PP nanocomposites (Table 3).[55−57] The melting (T_m) and crystalline temperature (T_c) of pristine PP appeared at 160.9 and 104.6 °C. After the addition of PANI nanofibers to the PP matrix, both T_m and T_c shifted

Table 3. DSC Peak Analyses of PP Nanocomposites Filled with PANI, r-PANI, and r-PANI/RGO[a]

sample	T_m (°C)	T_c (°C)	ΔH_m (J g^{-1})	X_c (%)[b]
pristine PP	160.9	104.6	86.9	41.6
PANI	158.7	102.7	79.7	39.3
r-PANI	165.1	108.5	79.1	39.0
RGO	172.3	114.1	76.0	38.6
r-PANI/RGO	169.4	111.1	78.2	37.5

[a]The concentration of all fillers is 10 vol % with respect to PP nanocomposites. [b]Degree of crystallinity (X_c) was obtained from DSC thermographs.

toward lower temperatures. However, T_m and T_c in the thermograph of PP/r-PANI shifted toward higher temperature than those of the pristine PP and PP/PANI (Table 3). This indicates that the counteranions of doping agents highly affect the thermal stability of the PANI structure.[61] Moreover, the PP nanocomposites filled with RGO and RGO/r-PANI cofiller exhibited higher T_m and T_c compared with those of the PP/r-PANI. These results suggest that the RGO sheets acted as nucleating agent for improving the thermal stability of PP nanocomposites.[32,46−48,62]

Figure 6b represents the Hoffman–Weeks plots for PP nanocomposites filled with different fillers.[63] The equilibrium temperature (T_m^0) for PP nanocomposites was calculated using the equation $T_m = \eta T_c + (1-\eta)T_m^0$, where T_m, T_c, and T_m^0 refer to the melting point, crystalline temperature, and equilibrium melting point of the PP nanocomposites, respectively.[63] A value of $\eta = 0$ means the perfectly stable PP crystal, while a value of $\eta = 1$ reflects that the PP crystals are inherently unstable.[63] PP nanocomposites filled with PANI, r-PANI, RGO, and r-PANI/RGO represented slightly higher η values than those of the pristine PP (Table S6). The results imply that the PP nanocomposites contain crystalline defects, and the crystalline defects are influenced by the fillers present in the PP matrices. T_m^0 (°C) of the nanocomposites increased as follows: PP/PANI (186.3) < pristine PP (187.4) < PP/r-PANI (194.3) < PP/r-PANI/RGO (200.8) < PP/RGO (205.0) (Table S6). Thus, the Hoffman–Weeks plots were in accordance with the DSC thermographs. Judging from these results, the r-PANI/RGO cofiller provides higher thermal properties than those of PANI, r-PANI, and RGO.

Conductivity, Dielectric, and Energy Harvesting Performances of PP/r-PANI/RGO Nanocomposite. The conductivity of fillers and PP nanocomposites filled with different fillers is shown in Figure 7. Conductivity was measured using the 4-point probe method, as described in the equation σ (S cm^{-1}) = $1/\rho = (\ln 2)/(\pi t)1/R$, where ρ, R, and t refer to the static resistivity, sheet resistivity, and thickness of the sample, respectively.[64] The conductivity of fillers increased as follows: PANI (16 S cm^{-1}) < RGO (40 S cm^{-1}) < r-PANI (156 S cm^{-1}) < r-PANI/RGO (220 S cm^{-1}), which is consistent with the WAXD, FT-IR, and XPS results (Figure 7a). The results indicate that the presence of RGO sheets and secondary doping of PANI can significantly increase the charge transport properties of PANI, which ultimately enhance the charge carrier mobility along the PANI chains.[30−32,50] When 10 vol % of these fillers was added into the PP matrices, the conductivity of PP nanocomposites filled with different fillers increased as follows: PP/PANI (0.072 S cm^{-1}) < PP/RGO (0.17 S cm^{-1}) < r-PANI (0.55 S cm^{-1}) < r-PANI/RGO (1.85 S cm^{-1}) (Figure 7b). These nanocomposites exhibited significantly enhanced conductivity compared with that of the pristine PP (5.52×10^{-15} S cm^{-1}), implying that the fillers were appropriately incorporated into the PP matrices and acted as conducting materials in the matrices.[32−37,42,62] To further understand how each phase contributed to the total conductivity of r-PANI/RGO cofiller, the conductivities of the r-PANI/RGO cofillers with different volume ratios of r-PANI to RGO ($v_{r\text{-PANI}}/v_{RGO}$) are summarized in Figure 7c. The $v_{r\text{-PANI}}/v_{RGO}$ ratios of 1:9, 3:7, 5:5, 7:3, and 9:1 correspond to the weight ratio of r-PANI to RGO ($w_{r\text{-PANI}}/w_{RGO}$) of 0.22:1.78, 0.62:1.38, 0.99:0.99, 1.38:0.62, and 1.78:0.22, respectively. The conductivity of the r-PANI/RGO with different $v_{r\text{-PANI}}/v_{RGO}$ ratios increased as follows: 1:9 (73 S cm^{-1}) < 3:7 (115 S cm^{-1})

DOI: 10.1021/acsami.5b05467
ACS Appl. Mater. Interfaces 2015, 7, 22301−22314

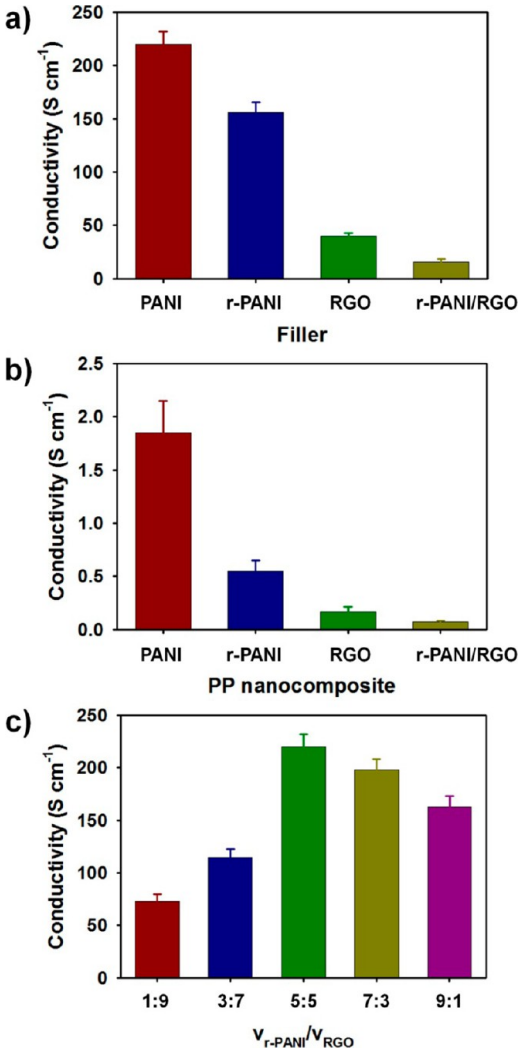

Figure 7. (a) Conductivity of r-PANI/RGO (red), r-PANI (blue), RGO (green), and PANI (olive green). (b) Conductivity of PP nanocomposites filled with r-PANI/RGO (red), r-PANI (blue), RGO (green), and PANI (olive green). (c) Conductivity of PP/r-PANI/RGO nanocomposites with different $v_{r\text{-PANI}}/v_{RGO}$ ratios: 1:9 (red), 3:7 (blue), 5:5 (green), 7:3 (olive green), and 9:1 (purple). The concentration of all fillers is 10 vol % with respect to PP nanocomposites.

< 9:1 (163 S cm^{-1}) < 7:3 (198 S cm^{-1}) < 5:5 (220 S cm^{-1}) (Figure 7c). This suggests that the optimal amounts of RGO can induce further enhancement in the π-conjugated r-PANI structures, allowing superior conductivity than those of the r-PANI and PANI nanofibers.[30−32,50]

Figure 8 represents the frequency dependencies of the dielectric constant (ε') and dielectric loss (ε'') of the PP nanocomposites filled with PANI, r-PANI, RGO, and r-PANI/RGO. In the 100 Hz to 1 MHz range, the ε' values of the samples decreased with increasing frequencies, suggesting that the dielectric impurities are present in the PP nanocomposites (Figure 8a).[4−9,65,66] At a frequency of 10^3 HZ, the ε' values of the PP nanocomposites filled with RGO, Ag NWs, PANI, r-PANI, and r-PANI/RGO were 11.0, 18.7, 20.7, 36.3, and 51.8, respectively, and these values were larger than that of the pristine PP (2.3). In addition, the enhancement of the dielectric constant of PP nanocomposites at low frequency may be related to the Maxwell−Wagner−Sillars (MWS) interfacial polarization effect.[65,66] In the PP matrices, the conductive r-PANI nanofibers and RGO sheets are isolated by insulating PP layers, and these conductive fillers form a number of microcapacitor structures throughout the nanocomposites, which result in the increased intensity of the local electric field.[65,66] For this reason, the dielectric constant of PP increased after the addition of PANI nanofibers and RGO sheets to the PP matrix. The dielectric losses of PP nanocomposites at a frequency of 10^3 Hz increased after the addition of fillers: pristine PP (4.9×10^{-4}) < PP/RGO (5.2×10^{-3}) < PP/r-PANI/RGO (9.3×10^{-3}) < PP/r-PANI (1.8×10^{-2}) < PP/PANI (2.5×10^{-2}) < Ag NWs (0.13) (Figure 8b). The higher dielectric losses of the samples filled with Ag NWs, PANI, r-PANI, RGO, and r-PANI/RGO cofiller than that of the pristine PP may be due to the leakage currents in the PP nanocomposites. The conductive fillers form conductive pathways in the polymer matrix, resulting in more leakage currents and higher dielectric losses in the PP nanocomposites.[8−12,42,59,65] In particular, despite the superior electrical properties of Ag NWs than the other fillers, the PP nanocomposite employing Ag NWs exhibited a lower dielectric constant and larger dielectric loss compared with those of the PANI, r-PANI, and r-PANI/RGO (Table 4). Thus, it is reasonable to assume that more electric energies are consumed to generate leakage currents during the polarization of the PP/Ag NWs nanocomposite than those of the PP nanocomposites filled with PANI, r-PANI, and r-PANI/RGO.[1−3,5,6,8−13,15−18,65,67,68] Figure 8c and 8d demonstrates the effects of r-PANI/RGO cofiller content on the dielectric properties of PP nanocomposites. The dielectric constants of PP nanocomposites containing r-PANI/RGO cofiller reached the maximum value (51.8) at the cofiller loading of 10 vol % and decreased after adding cofillers at contents that exceeded 10 vol %: pristine PP (2.3) < 1 vol % (5.3) < 2.5 vol % (17.6) < 5 vol % (35.3) < 12 vol % (46.0) < 10 vol % (51.8) (Figure 8c). As the cofiller content increases, the content of PP that occupies the less crystalline polymer region increases, which may induce more charge traps and higher space charge densities.[33−37,42,62] However, the excessive filler loading causes the imperfect filler packing and aggregation of fillers in the polymer matrices, which, in turn, would reduce the interfacial polarization of nanocomposites.[65,66] Hence, the optimal cofiller content for PP nanocomposite was chosen as 10 vol %. The high filler content of r-PANI/RGO resulted in higher dielectric losses as follows: pristine PP (4.9×10^{-4}) < 1 vol % (2.4×10^{-3}) < 2.5 vol % (4.4×10^{-3}) < 5 vol % (6.6×10^{-3}) < 10 vol % (9.3×10^{-3}) < 12 vol % (1.6×10^{-2}) (Figure 8d). This reconfirms that the higher cofiller loading has increased the leakage currents in the PP nanocomposites, which may increase the dielectric loss of nanocomposites.[65,66] Despite the increase in dielectric loss of the nanocomposites, the PP/r-PANI/RGO with 10 vol % cofiller exhibited more than 10 times lower dielectric loss compared with that of the conventional PVDF (0.11).[1−11,16] Judging from these results, the dielectric properties of PP filled with r-PANI/RGO make them suitable for use as energy-harvesting devices. For further insights into the effect of each phase in the PP/r-PANI/RGO nanocomposites, ε' and ε'' of the PP nanocomposites filled with different $v_{r\text{-PANI}}/v_{RGO}$ ratios are represented in Figure S3. As seen, the dielectric constant of PP/r-PANI/RGO reached the maximum at a $v_{r\text{-PANI}}/v_{RGO}$ ratio of 5:5 and decreased when the volume fraction of r-PANI increased to >5 vol % (Figure S3a). The dielectric constant of PP/r-PANI/RGO nanocomposites

DOI: 10.1021/acsami.5b05467
ACS Appl. Mater. Interfaces 2015, 7, 22301−22314

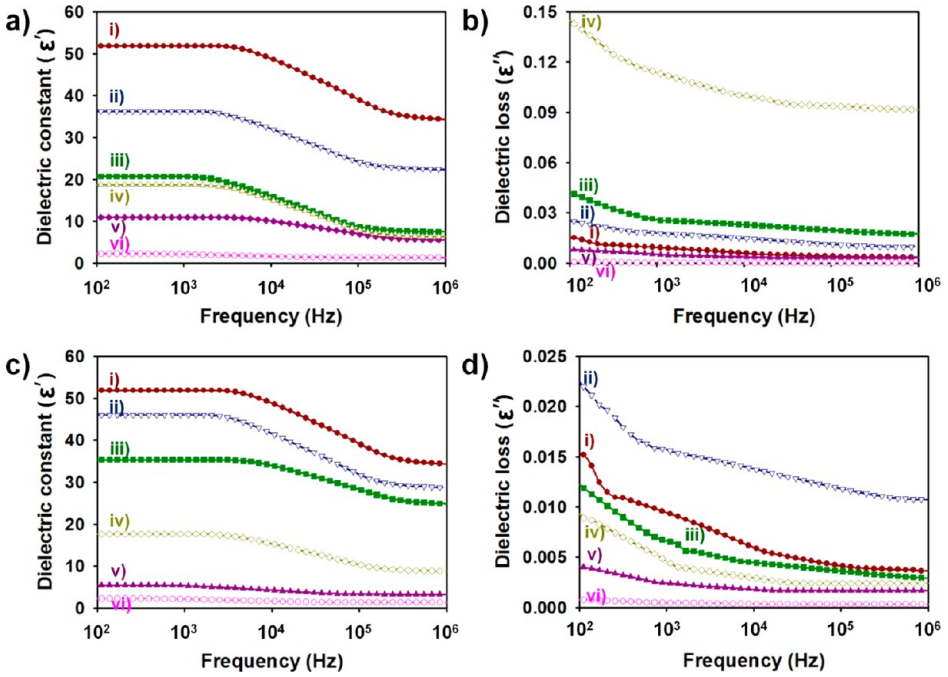

Figure 8. Dependences of (a) dielectric constants and (b) dielectric losses of PP nanocomposites filled with r-PANI/RGO (red), r-PANI (blue), PANI (green), Ag NWs (olive green), RGO (purple), and pristine PP (pink) on frequency from 10^2 to 10^6 Hz. The concentration of all fillers is 10 vol % with respect to PP nanocomposites. Dependences of (c) dielectric constants and (d) dielectric losses of PP nanocomposites filled with different r-PANI/RGO cofiller content (0−12.5 vol %) on frequency from 10^2 to 10^6 Hz: 10 vol % (red), 12.5 vol % (blue), 5 vol % (green), 2.5 vol % (olive green), 1 vol % (purple), and pristine PP (pink).

Table 4. Summary of Electrical Properties of Pristine PP, PANI, r-PANI, r-PANI/RGO, and Ag NWs and Dielectric Properties of PP Nanocomposites Filled with PANI, r-PANI, r-PANI/RGO, and Ag NWs[a]

	electrical properties of fillers		dielectric properties of nanocomposites	
sample	σ (S cm^{-1})[b]	R (Ω)[c]	ε'[d]	ε''[e]
PP	5.52×10^{-15}	4.00×10^{16}	2.3	4.9×10^{-4}
RGO	40	5.52	11	5.2×10^{-3}
PANI	16	13.8	20.7	2.5×10^{-2}
r-PANI	156	1.41	36.3	1.8×10^{-2}
r-PANI/RGO	220	1.00	51.8	9.3×10^{-3}
Ag NWs	1530	0.144	18.7	0.13

[a]The concentration of all fillers is 10 vol % with respect to PP nanocomposites. [b]Fillers for conductivity measurements have been prepared as 10 μm thickness films. [c]Fillers for surface resistance measurements have been prepared as 10 μm thickness films. [d]Dielectric constant of all samples were measured at a frequency of 10^3 Hz. [e]Dielectric loss of all samples was measured at a frequency of 10^3 Hz.

with different $v_{\text{r-PANI}}/v_{\text{RGO}}$ ratios at a frequency of 10^3 Hz increased as follows: 1:9 (13.5) < 3:7 (18.1) < 9:1 (38.4) < 7:3 (43.3) < 5:5 (51.8). This implies that the appropriate combination of r-PANI and RGO resulted in more effective formation of the microstructures and higher space charge densities throughout the PP matrices, giving rise to the improved dielectric constant of PP nanocomposite.[1−3,5,6,8−13,15−18,65] With increasing $v_{\text{r-PANI}}/v_{\text{RGO}}$ ratio, the dielectric loss of PP/r-PANI/RGO nanocomposites increased as follows: 1:9 (6.1×10^{-4}) < 3:7 (7.9×10^{-3}) < 5:5 (9.3×10^{-3}) < 7:3 (1.2×10^{-2}) < 9:1 (1.7×10^{-2}) (Figure S3b). The results indicate the RGO sheets may cause less leakage currents due to their larger grain sizes with smaller numbers of grain boundaries in the PP matrix compared to that of the r-PANI nanofibers.[1−3,5,6,8−13,15−18,65] Judging from these results, the optimal $v_{\text{r-PANI}}/v_{\text{RGO}}$ ratio for PP/r-PANI/RGO nanocomposite was chosen as 5:5 (0.99:0.99, $w_{\text{r-PANI}}/w_{\text{RGO}}$).

To evaluate the energy-harvesting performance of the PP nanocomposites, the energy densities of the samples were estimated from the polarization−electric field (P−E) hysteresis loops (Figure 9). The ideal dielectric material demonstrates a linear polarization response, which is exactly proportional to the external electric field (E) when the material is polarized. Therefore, the energy density of the linear dielectric capacitors can be defined in the equation $\kappa_{\text{eff}}\varepsilon_0 E_b^2/2$, where κ_{eff} refers to the effective permittivity of the sample, E_b denotes the breakdown strength, and ε_0 indicates the vacuum permittivity (8.85×10^{-12} nF m^{-1}).[1−3,5,6,8−13,15−18] In contrast to the ideal dielectric polarization, the ferroelectric materials exhibit a nonlinear and spontaneous nonzero polarization even at an E of 0; the spontaneous polarization is reserved by applying sufficient electric field in the opposite direction. Considering the practical application of ferroelectric capacitors, the real energy density of PP nanocomposites could be calculated using the equation $U_e = \int E\,dP$, where E and P refer to the electric field and polarization of the samples, respectively.[1−3,5,6,8−13,15−18] Figure 9a represents P−E hysteresis loops for PP nanocomposites filled with 10 vol % of fillers at room temperature. As seen, the P−E hysteresis loops of samples clearly demonstrate the nonlinear polarization responses and the saturated polarization (P_s) of PP (0.61 μC cm^{-2}) have been improved after the addition of RGO (2.80 μC cm^{-2}), Ag NWs (4.65 μC cm^{-2}), PANI (5.18 μC cm^{-2}), r-PANI (9.31 μC cm^{-2}), and r-PANI/RGO cofiller (13.3 μC cm^{-2}). Moreover, the PP nanocomposites filled with r-PANI/RGO cofiller, r-PANI, PANI, and RGO exhibited a larger

DOI: 10.1021/acsami.5b05467
ACS Appl. Mater. Interfaces 2015, 7, 22301−22314

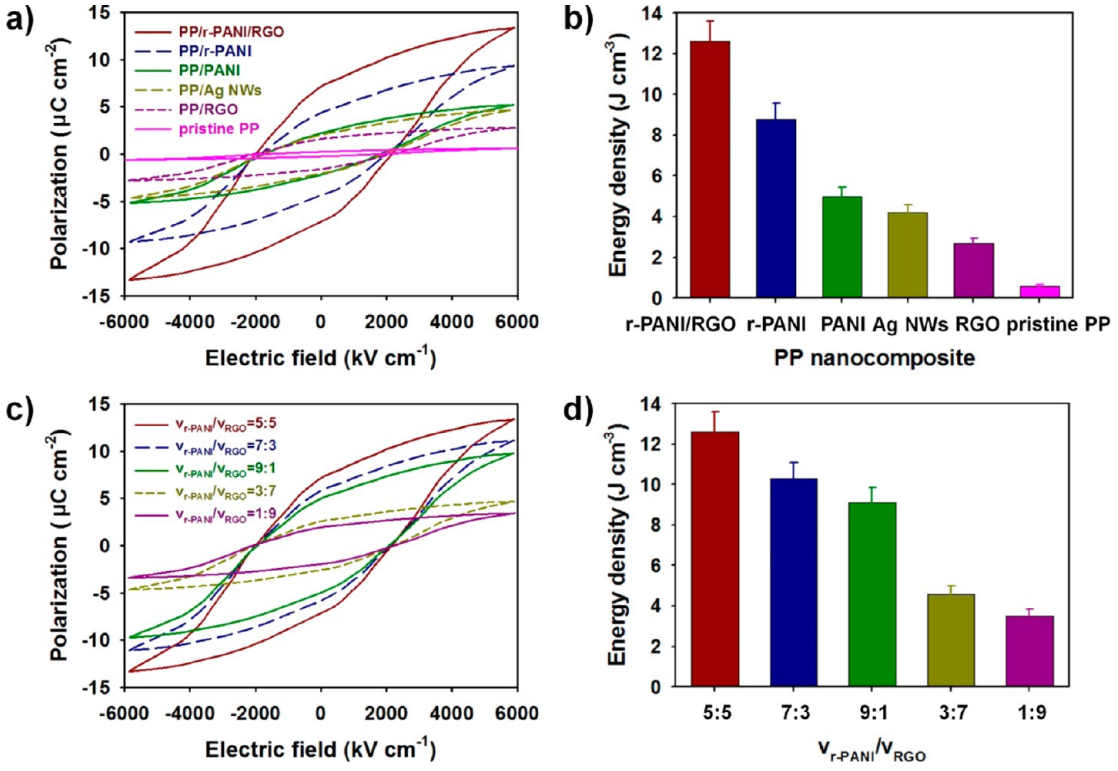

Figure 9. (a) Polarization–electric field (P–E) hysteresis loops and (b) energy density of PP nanocomposites filled with r-PANI/RGO (red), r-PANI (blue), PANI (green), Ag NWs (olive green), RGO (purple), and pristine PP (pink). (c) Polarization–electric field (P–E) hysteresis loops and (d) energy density of PP/r-PANI/RGO nanocomposites with different $v_{r\text{-PANI}}/v_{RGO}$ ratios: 5:5 (red), 7:3 (blue), 9:1 (green), 3:7 (olive green), and 1:9 (purple). The concentration of all fillers is 10 vol % with respect to PP nanocomposites.

remnant polarization (P_r) and P_r/P_s ratio compared to that of the pristine PP (Table 5). Such enhancements in the ferroelectric properties of PP nanocomposites are possibly due to the enhanced charge traps and higher space charge densities caused by the fillers.[1−3,5,6,8−13,15−18,65] More specifically, the r-PANI and PANI nanofibers have shown larger polarization responses than the RGO, indicating that the secondarily doped r-PANI nanofibers with enhanced charge carrier mobility can generate more charge traps and higher charge densities throughout the PP nanocomposites.[29,32−37,42,50,62,65,66] However, the P_r/P_s ratio and breakdown strength of PP/RGO was slightly higher than those of the nanocomposites employing the r-PANI and PANI nanofibers (Table 5). Because of the larger grain size of RGO, the PP/RGO nanocomposite may induce a lower number of grain boundaries compared to the PP nanocomposites employing r-PANI, PANI, and Ag NWs.[33−37,42,62,65,66] Such decrease in the number of grain boundaries may minimize the polarization losses and leakage currents during the polarization of nanocomposites, thereby preventing a decrease of the breakdown strength.[1−3,5,6,8−13,15−18,33−37,42,62,65,66] The breakdown strength electric fields of the PP nanocomposites filled with 10 vol % Ag NWs, RGO, PANI, r-PANI, and r-PANI/RGO were measured as 5.78×10^3, 5.87×10^3, 5.82×10^3, 5.84×10^3, and 5.86×10^3 kV cm^{-1}, respectively, and these values were slightly lower than that of the pristine PP ($E \approx 5.97 \times 10^3$ kV cm^{-1}). The decrease in breakdown voltage of the nanocomposites may be due to the structural defects in the PP region closest to the fillers.[33−37] Despite the decreases in breakdown strength of the PP nanocomposites, it was evident that the combination of r-PANI and RGO was more effective to minimize the losses in breakdown voltage than those of the r-PANI, PANI, and Ag NWs. In addition, the PP nanocomposites provided a higher breakdown strength than that of the PVDF ($E \approx 4.0 \times 10^3$ kV cm^{-1}), making them suitable for capacitor applications. Given the smaller decreases in the breakdown strength, the PP/r-PANI/RGO nanocomposite can be polarized at a higher electric field than those of the nanocomposites filled with r-PANI and PANI nanofibers without causing a significant leakage current, giving rise to an increased energy density of the nanocomposite.[1−3,5,6,8−13,15−18] After the incorporation of fillers into PP matrices, the energy density of the samples increased as follows (J cm^{-3}): pristine PP (0.58) < PP/RGO (2.7) < PP/PANI (5.0) < PP/r-PANI (8.8) < PP/r-PANI/RGO (12.6) (Figure 9b, Table 5). The increases in the energy densities of nanocomposites can be explained by the following points. (1) As the secondarily doped r-PANI has higher charge carrier mobility than that of the primarily doped PANI, the PP/

Table 5. Ferroelectric Properties of PP Nanocomposites Filled with RGO, PANI, r-PANI, r-PANI/RGO, and Ag NWs

sample	P_s[a]	P_r[a]	P_r/P_s[a]	E_b (kV cm^{-1})[a]	energy density (J cm^{-3})[a]
pristine PP	0.61	0.24	0.40	5.97×10^3	0.58 ± 0.10
RGO	2.80	1.61	0.58	5.87×10^3	2.7 ± 0.25
PANI	5.18	2.20	0.43	5.82×10^3	5.0 ± 0.45
r-PANI	9.31	4.36	0.47	5.84×10^3	8.8 ± 0.75
r-PANI/RGO	13.3	7.14	0.54	5.86×10^3	12.6 ± 1.0
Ag NWs	4.65	2.05	0.44	5.78×10^3	4.2 ± 0.40

[a]These values were estimated from the P–E hysteresis loops.

DOI: 10.1021/acsami.5b05467
ACS Appl. Mater. Interfaces 2015, 7, 22301−22314

r-PANI provides more charge space densities compared with that of the PP/PANI. (2) PANI nanofibers generate more charge traps in the PP matrices than that of the RGO sheets, while the RGO provides better breakdown strength compared with that of the PANI and r-PANI. (3) Therefore, the combination of r-PANI and RGO could result in the largest polarization displacement among the other samples containing each element alone. To further clarify the factors on the ferroelectric enhancement of the PP/r-PANI/RGO nanocomposite, the *P*–*E* hysteresis loops of the PP nanocomposites with different $v_{\text{r-PANI}}/v_{\text{PANI}}$ ratios are represented in Figure 9c. The breakdown strength and P_r/P_s ratio of nanocomposites increased with RGO loading, reconfirming that the RGO sheets may play an important role to minimize the leakage currents and polarization losses of the PP nanocomposites employing the r-PANI nanofibers (Table 6).[1−3,5,6,8−13,15−18,33−37,42,62,65,66]

Table 6. Ferroelectric Properties of PP/r-PANI/RGO Nanocomposites with Different $v_{\text{r-PANI}}/v_{\text{RGO}}$ Ratios

$v_{\text{r-PANI}}/v_{\text{RGO}}$	P_s[a]	P_r[a]	P_r/P_s[a]	E_b (kV cm^{-1})[a]	energy density (J cm^{-3})[a]
5:5	13.3	7.14	0.54	5.86×10^3	12.6 ± 1.0
7:3	11.1	5.82	0.52	5.85×10^3	10.3 ± 0.80
9:1	9.74	4.98	0.51	5.84×10^3	9.1 ± 0.75
3:7	4.66	2.58	0.55	5.86×10^3	4.6 ± 0.40
1:9	3.42	1.95	0.57	5.87×10^3	3.5 ± 0.35

[a]These values were estimated from the P–E hysteresis loops.

The maximum values of P_s and P_r have been reached at a $v_{\text{r-PANI}}/v_{\text{PANI}}$ of 5:5 (0.99:0.99, $w_{\text{r-PANI}}/w_{\text{PANI}}$), suggesting that the r-PANI nanofibers, which have better charge carrier mobility than the RGO sheets, are in charge of generating the charge traps and local electric field throughout the nanocomposites. When the volume fraction of r-PANI nanofibers increased to >5 vol %, the polarization responses of nanocomposites became lower compared to that of the sample with a $v_{\text{r-PANI}}/v_{\text{PANI}}$ ratio of 5:5 (Table 6). These results reconfirm that the RGO sheets not only reduce the leakage currents and polarization losses of the nanocomposites but also further extend the π-conjugated structure of r-PANI/RGO nanocomposites for generating more charge traps throughout the PP matrices.[29,32−37,42,50,62,65,66] The energy density values of PP nanocomposites with different $v_{\text{r-PANI}}/v_{\text{PANI}}$ ratios of r-PANI and RGO were calculated from the *P*–*E* hysteresis loops, and the energy density of the samples increased as follows (J cm^{-3}): 1:9 (3.5) < 3:7 (4.6) < 9:1 (9.1) < 7:3 (10.3) < 5:5 (12.6) (Figure 9d, Table 6). This suggests that the appropriate volume ratio of r-PANI and RGO gives rise to the effective utilization of each phase, thereby significantly improving the energy density of PP nanocomposites.[1−3,5,6,8−13,15−18,33−37,42,62] To identify the optimal adding amounts of r-PANI/RGO cofillers to obtain the highest ferroelectric properties, the *P*–*E* hysteresis loops of the PP/r-PANI/RGO nanocomposites with different cofiller content are shown in Figure S4a. The maximum values of P_s, P_r, and P_r/P_s have been reached at the cofiller loading of 10 vol %, suggesting that the r-PANI/RGO cofiller creates a number of microcapacitor structures to enhance the local electric field (Table S7). However, such increased microcapacitor structures also mean an increase of structural defects throughout the PP nanocomposites, resulting in a decrease of the breakdown strength.[33−37,42,62,65,66] Therefore, the breakdown strength of PP/r-PANI/RGO nanocomposites decreased with increasing cofiller content (Table S7). Furthermore, the excessive filler loading causes more consumption of the electric energy in the formation of leakage currents during the polarization of the PP/r-PANI/RGO nanocomposites, resulting in a decrease of the polarization degree.[1−3,5,6,8−13,15−18,33−37,42,62,65,66] Thus, the energy density of PP/r-PANI/RGO with 10 vol % cofiller was larger than that of the nanocomposite with 12 vol % cofiller (Figure S4b). Considering these results, the r-PANI/RGO cofiller with an optimal cofiller content can be an efficient means to improve the energy-harvesting properties of the PP nanocomposites.[32−37,42,62,65,66]

CONCLUSIONS

We fabricated PP nanocomposite filled with r-PANI nanofibers and RGO sheets via simple solution processes. The changes in crystallinity of the PP nanocomposites were monitored by XRD, POM, and DSC. Although there was no phase transformation from α- to β-form PP, the T_m and T_c of PP shifted toward higher temperatures with 10 vol % loading of r-PANI/RGO cofiller. In addition, the sizes and growth rates of spherulites were reduced after the addition of r-PANI and RGO sheets. The charge transport properties of fillers were carefully characterized by XRD, FT-IR, and XPS spectroscopies. Results suggest that the r-PANI/RGO cofiller was efficient to enhance the protonation level and conjugation length of PANI chains. These enhancements of the charge transport properties were in good agreement with the conductivity of fillers and PP nanocomposites. The PP/r-PANI/RGO exhibited an enhanced dielectric constant of $\varepsilon' \approx 51.8$ and comparable dielectric loss of $\varepsilon'' \approx 9.3 \times 10^{-3}$ at a frequency of 10^3 Hz compared with that of the pristine PP ($\varepsilon' \approx 2.3$ and $\varepsilon'' \approx 4.9 \times 10^{-4}$). Moreover, the PP/r-PANI/RGO nanocomposite demonstrated improved energy density ($U_e \approx 12.6$ J cm^{-3}) and comparable breakdown voltage ($E \approx 5.86 \times 10^3$ kV cm^{-1}) relative to that of the pristine PP ($E \approx 5.97 \times 10^3$ kV cm^{-1}). The procedure described herein demonstrates that the use of PP/r-PANI/RGO ternary nanocomposite can be used to produce high-performance capacitors with greater performance compared with that of the PVDF and PP.

EXPERIMENTAL SECTION

Materials. Aniline (99.0%), ammonium persulfate (APS, 98.0%), polypropylene (PP, molecular weight ca. 250 000), poly(ethylene oxide) (PEO, molecular weight ca. 200 000), toluene ($C_6H_5CH_3$, 99.5%), graphite, natural flake graphite, sodium carbonate (Na_2CO_3, 99.5%), sodium nitrate ($NaNO_3$, 99%), hydrazine monohydrate ($N_2H_4{\cdot}H_2O$, 98%), nitric acid (HNO_3, 70%), and silver nanowires (Ag NWs, 0.5% in isopropanol with a diameter of 60 ± 10 nm and length of 10 ± 5 μm) were purchased from Sigma-Aldrich (St. Louis, MO). Potassium permanganate ($KMnO_4$, 99.3%) and phosphorus pentoxide (P_2O_5, extra pure) were acquired from Junsei Chemical Co. (Tokyo, Japan). Potassium persulfate ($K_2S_2O_8$, 99%) was acquired from Kanto Chemical Co. (Tokyo, Japan). Sulfuric acid (H_2SO_4, 95%), sodium hydroxide (NaOH, 99%), hydrogen peroxide (H_2O_2, 30−35.5%), and hydrochloric acid (HCl, 35−37%) were obtained. *m*-Cresol was purchased from Tokyo Chemical Industry (Tokyo, Japan). Carbon nanofibers (CNFs; NEXCARB-H, <50 nm) were acquired from Suntel Co. (Korea).

Synthesis of RGO Solutions. RGO solutions were prepared according to modified Hummers and Ruoff methods.[43,44] To preoxidize the natural graphite powders, 5 g of graphite powder, 2.5 g of P_2O_5, and 2.5 g of $K_2S_2O_8$ were added into 30 mL of H_2SO_4; the mixture solution was heated at 90 °C for 6 h. The mixture solution was washed with water through a cellulose acetate filter (Whatmann Inc.,

DOI: 10.1021/acsami.5b05467
ACS Appl. Mater. Interfaces 2015, 7, 22301−22314

USA). As-prepared preoxidized powder was dried in a vacuum oven at room temperature for 24 h. The preoxidized graphites were mixed with a mixture of 2.5 g of $NaNO_3$ and 120 mL of H_2SO_4, followed by vigorous stirring for 30 min in an ice bath. A 15.0 g amount of $KMnO_4$ was added to the mixture solution at lower than <20 °C, and then the solution was heated at 35 °C for 4 h, which resulted in the formation of a brownish gray paste. After the addition of 600 mL of distilled water and 25 mL of H_2O_2 solution to the brownish gray paste, the color of the paste changed to yellow. The yellowish paste was washed with 5 wt % HCl and distilled water several times to balance the pH of the solution to 7. To exfoliate graphitic oxide into graphene oxide (GO), the solution was sonochemically treated for 1 h. To exclude residues, the samples have been centrifuged at 10 000 rpm for 30 min. As-prepared GO powder (1 mg mL^{-1}, in distilled water) was redispersed into distilled water. To reduce the aqueous solution of GO, hydrazine monohydrate (1/1000 v/v vs water) was added to a GO solution with vigorous stirring at 95 °C for 1 h. The reduced graphene oxide (RGO) solution was washed with excess distilled water; the washed RGO sample was dried in a vacuum oven at 25 °C for 24 h. Consequently, the dried RGO (40 mg mL^{-1} in *m*-cresol, 3.7 wt % with respect to *m*-cresol) was dissolved in *m*-cresol (*m*-cresol:RGO = 95:5 by volume).

Synthesis of r-PANI Nanofibers. Redoped polyaniline (r-PANI) nanofibers were synthesized using the combining method of chemical oxidation polymerization and secondary doping.[29−32] Aniline (1 g) was doped with 200 mL of 0.2 M hydrochloric acid (HCl) solution, followed by vigorous stirring for 10 min. The polymerization of aniline was initiated by adding 1.2 g of APS as an oxidizing agent for 1 h at room temperature. To obtain the precipitates of greenish PANI emeraldine salt (ES), as-prepared PANI solution was washed with water, ethanol, and acetone. A 200 mL amount of 0.5 M ammonia (NH_3) solution was used as a reducing agent to remove the primary dopant of PANI ES. The reduced PANI emeraldine base (EB) was washed with water, ethanol, and acetone; the washed PANI EB was redoped with 0.5 M camphorsulfonic acid (CSA) solution. r-PANI solution was prepared by adding r-PANI powders (40 mg mL^{-1}) to a mixture of *m*-cresol and $CHCl_3$ (*m*-cresol:$CHCl_3$ = 4:1 by volume). As-prepared r-PANI solution was sonochemically treated for 24 h to increase the solubility of r-PANI powders in the *m*-cresol/$CHCl_3$ cosolvent.

Fabrication of PP/r-PANI/RGO Nanocomposite. To prepare r-PANI/RGO cofiller solution, 1.0 mL of r-PANI solution was mixed with 1.0 mL of RGO solution, and the mixture of r-PANI/RGO was vigorously stirred for 1 h, followed by sonication treatment for 30 min. A 1.0 mL amount of r-PANI/RGO solution (1:1, v/v) and 4.0 g of PP were dispersed in 18 mL of toluene through vigorous stirring for 12 h. To promote the dispersions of the r-PANI nanofibers and RGO sheets in the PP matrix, the mixed solutions were sonochemically treated using an ultrasonicator (VCX 500, Sonics & Materials. Inc. USA) for 1 h. The vol % of r-PANI/RGO in the PP nanocomposite was calculated using eq 1

$$\frac{v_{\text{r-PANI}} + v_{\text{RGO}}}{v_{\text{r-PANI}} + v_{\text{RGO}} + v_{\text{PP}}} \times 100\% = \frac{1.0\ \text{mL} + 1.0\ \text{mL}}{18\ \text{mL} + 1.0\ \text{mL} + 1.0\ \text{mL}} \times 100\% = 10\ \text{vol}\% \quad (1)$$

where $v_{\text{r-PANI}}$, v_{RGO}, and v_{PP} refer to the volume of r-PANI (1.0 mL, 40 mg mL^{-1} in *m*-cresol/$CHCl_3$, 3.4 wt % with respect to *m*-cresol/$CHCl_3$ mixture), RGO (1.0 mL, 40 mg mL^{-1} in *m*-cresol, 3.7 wt % with respect to *m*-cresol), and PP (18 mL, 0.22 g mL^{-1} in toluene, 20.3 wt % with respect to toluene) solutions, respectively. The wt % of r-PANI/RGO cofiller in the PP nanocomposite was estimated using eq 2

$$\frac{(v_{\text{r-PANI}} \times d_{\text{r-PANI}}) + (v_{\text{RGO}} \times d_{\text{RGO}})}{(v_{\text{r-PANI}} \times d_{\text{r-PANI}}) + (v_{\text{RGO}} \times d_{\text{RGO}}) + (v_{\text{PP}} \times d_{\text{PP}})} \times 100\ \text{wt}\% = 1.98\ \text{wt}\% \quad (2)$$

where $d_{\text{r-PANI}}$, d_{RGO}, and d_{PP} refer to the density of r-PANI (1.0 mL, 40 mg mL^{-1} in *m*-cresol/$CHCl_3$, 3.4 wt % with respect to *m*-cresol/$CHCl_3$ mixture), RGO (1.0 mL, 40 mg mL^{-1} in *m*-cresol, 3.7 wt % with respect to *m*-cresol), and PP (18 mL, 0.22 g mL^{-1} in toluene, 20.3 wt % with respect to toluene) solutions, respectively. The solution of PP/r-PANI/RGO nanocomposite was deposited onto a glass substrate using the spin-coating method (EC101D, Headway Research, Garland, TX, USA), and the sample was dried in a vacuum oven at 25 °C for 24 h. The spin-coating process resulted in a film thickness of about 40 μm.

Instrumental Analyses. Images of the fillers and PP nanocomposites were obtained with a transmission electron microscope (TEM, LIBRA 120, Carl Zeiss, Germany). Fourier transform infrared (FT-IR) spectra of the samples were acquired with Frontier FT-IR spectrometers (PerkinElmer Inc. Waltham, MA, USA). X-ray photoelectron spectroscopy (XPS) spectra was obtained using an X-ray photoelectron spectrometer (XPS; AXIS-His, Kratos/Shimadzu, Kyoto, Japan). X-ray diffractograms (XRDs) of the fillers and PP nanocomposites were recorded on a SmartLab X-ray diffractometer (Rigaku Co., Tokyo, Japan). Differential scanning calorimetry (DSC) data of the PP nanocomposites were recorded on a differential scanning calorimeter (Q1000, TA Instruments, Austin, TX, USA) with a heating rate of 10 °C min^{-1} and a cooling rate of 8 °C min^{-1} from 25 to 240 °C under nitrogen atmosphere. The conductivity of the fillers and PP nanocomposites was obained using a four-point probe system (Mode Systems Co., Korea) equipped with a currentsource meter (Keithley 2400, Keithley Co., USA). The dielectric properties of the PP nanocomposites were recorded on a frequency response analyzer (FRA1260, Solartron-Schlumberger, Farnborough, UK). The polarization−electric field (*P*−*E*) curves and energy densities of the PP nanocomposites were measured using a function generator (FG300, Yokogawa, Japan), a digital oscilloscope (DL7100, Yokogawa, Japan), and a voltage amplifier (610E, Trek, USA).

■ ASSOCIATED CONTENT

Supporting Information

The Supporting Information is available free of charge on the ACS Publications website at DOI: 10.1021/acsami.5b05467.

Hansen solubility parameters for *m*-cresol, chloroform, and toluene, FT-IR spectra of GO and RGO for different reduction times, characteristic bands with specific vibrational modes of GO, r-PANI, and PP, fully XPS scanned spectra and XPS elemental analyses of RGO, PANI, d-PANI, r-PANI, and r-PANI/RGO, and Hoffman−Weeks analyses for PP nanocomposites filled with different fillers; dependences of dielectric constants and dielectric losses on frequency from 10^2 to 10^6 Hz, polarization−electric field (*P*−*E*) hysteresis loops, energy density, and summary of ferroelectric properties of PP/r-PANI/RGO nanocomposites filled with different $v_{\text{r-PANI}}/v_{\text{RGO}}$ ratios (PDF)

■ AUTHOR INFORMATION

Corresponding Author

*E-mail: jsjang@plaza.snu.ac.kr.

Notes

The authors declare no competing financial interest.

■ ACKNOWLEDGMENTS

This work was supported by the Global Frontier R&D Program on Center for Multiscale Energy System funded by the National Research Foundation under the Ministry of Education, Science and Technology, Korea (2011-0031573).

DOI: 10.1021/acsami.5b05467
ACS Appl. Mater. Interfaces 2015, 7, 22301−22314

REFERENCES

(1) Zhang, Z. C.; Chung, T. C. Fluoro-Terpolymer Based Capacitors Having High Energy Density, Low Energy Loss, and High Pulsed Charge-Discharge Cycles. *Macromolecules* **2007**, *40*, 783−785.

(2) Zhang, Z. C.; Chung, T. C. The Structure-Property Relationship of PVDF-Based Polymers with Energy Storage and Loss under Applied Electric Fields. *Macromolecules* **2007**, *40*, 9391−9397.

(3) Cauda, V.; Stassi, S.; Bejtka, K.; Canavese, G. Nanoconfinement: An Effective Way to Enhance PVDF Piezoelectric Properties. *ACS Appl. Mater. Interfaces* **2013**, *5*, 6430−6437.

(4) Mendes, F.; Costa, C. M.; Caparros, C.; Sencadas, V.; L-Mendez, S. Effect of Filler Size and Concentration on The Structure and Properties of Poly(vinylidene fluoride)/$BaTiO_3$ Nanocomposites. *J. Mater. Sci.* **2012**, *47*, 1378−1388.

(5) Kim, P.; Doss, N. M.; Tillotson, J. P.; Hotchikiss, P. J.; Pan, M.-J.; Marder, S. R.; Li, J.; Calame, J. P.; Perry, J. W. High Energy Density Nanocomposites Based on Surface-modified $BaTiO_3$ and a Ferroelectric Polymer. *ACS Nano* **2009**, *3*, 2581−2592.

(6) Zhou, T.; Zha, J.-W.; Cui, R.-Y.; Fan, B.-H.; Yuan, J.-K.; Dang, Z.-M. Improving Dielectric Properties of $BaTiO_3$/Ferroelectric Polymer Composites by Employing Surface Hydroxylated $BaTiO_3$ Nanoparticles. *ACS Appl. Mater. Interfaces* **2011**, *3*, 2184−2188.

(7) Greforio, R., Jr.; Cestari, M.; Bernardino, F. E. Dielectric Behaviour of Thin Films of β-PVDF/PZT and β-PVDF/$BaTiO_3$ Composites. *J. Mater. Sci.* **1996**, *31*, 2925−2930.

(8) Guo, N.; DiBenedetto, S. A.; Tewari, P.; Lanagan, M. T.; Ratner, M. A.; Marks, T. J. Nanoparticle, Size, Shape, and Interfacial Effects on Leakage Current Density, Permittivity, and Breakdown Strength of Metal Oxide-Polyolefin Nanocomposites: Experiment and Theory. *Chem. Mater.* **2010**, *22*, 1567−1578.

(9) Chung, T. M. Functionalization of Polypropylene with High Dielectric Properties: Applications in Electric Energy Storage. *Green Sustainable Chem.* **2012**, *2*, 29−37.

(10) Li, Z.; Fredin, L. A.; Tewari, P.; DiBenedetto, S. A.; Lanagan, M. T.; Ratner, M. A.; Marks, T. J. In Situ Catalytic Encapsulation of Core-Shell Nanoparticles Having Variable Shell Thickness: Dielectric and Energy Storage Properties of High-Permittivity Metal Oxide Nanocomposites. *Chem. Mater.* **2010**, *22*, 5154−5164.

(11) Fredin, L. A.; Li, Z.; Ratner, M. A.; Lanagan, M. T.; Marks, T. J. Enhanced Energy Storage and Suppressed Dielectric Loss in Oxide Core−Shell−Polyolefin Nanocomposites by Moderating Internal Surface Area and Increasing Shell Thickness. *Adv. Mater.* **2012**, *24*, 5946−5953.

(12) Yuan, X.; Matsuyama, Y.; Chung, T. C. Synthesis of Functionalized Isotactic Polypropylene Dielectrics for Electric Energy Storage Applications. *Macromolecules* **2010**, *43*, 4011−4015.

(13) Ma, R.; Baldwin, A. F.; Wang, C.; Offenbach, I.; Cakmak, M.; Ramprasad, R.; Sotzing, G. A. Rationally Designed Polyimides for High-Energy Density Capacitor Applications. *ACS Appl. Mater. Interfaces* **2014**, *6*, 10445−10451.

(14) Díez-Pascual, A. M.; Díez-Vicente, A. L. High-Performance Aminated Poly(phenylene sulfide)/ZnO Nanocomposites for Medical Applications. *ACS Appl. Mater. Interfaces* **2014**, *6*, 10132−10145.

(15) Tang, H.; Zhou, Z.; Sodano, H. A. Relationship Between $BaTiO_3$ Nanowire Aspect Ratio and The Dielectric Permittivity of Nanocomposites. *ACS Appl. Mater. Interfaces* **2014**, *6*, 5450−5455.

(16) Liu, S.; Zhai, J. Improving The Dielectric Constant and Energy Density of Poly(vinylidene fluoride) Composites Induced by Surface-modified $SrTiO_3$ Nanofibers by Polyvinylpyrrolidone. *J. Mater. Chem. A* **2015**, *3*, 1511−1517.

(17) Lee, S. W.; Han, J. H.; Han, S.; Lee, W.; Jang, J. H.; Seo, M.; Kim, S. K.; Dussarrat, C.; Gatineau, J.; Min, Y.-S.; Hwang, C. S. Atomic Layer Deposition of $SrTiO_3$ Thin Films with Highly Enhanced Growth Rate for Ultrahigh Density Capacitor. *Chem. Mater.* **2011**, *23*, 2227−2236.

(18) Lee, W.; Han, J. H.; Jeon, W.; Yoo, Y. W.; Lee, S. W.; Kim, S. K.; Ko, C.-H.; Lansalot-Matras, C.; Hwang, C. S. Atomic Layer Deposition of $SrTiO_3$ Films with Cyclopentadienyl-based Precursors for Metal−insulator−metal Capacitors. *Chem. Mater.* **2013**, *25*, 953−961.

(19) Feng, Z.; Zhao, X.; Luo, H. Large Pyroelectric Effect in Relaxor-based Ferroelectric $Pb(Mg_{1/3}Nb_{2/3})O_3$−$PbTiO_3$ Single Crystals. *J. Am. Ceram. Soc.* **2006**, *89*, 3437−3440.

(20) Zhou, Y.; Han, S.-T.; Xu, Z.-X.; Yang, X.-B.; Ng, H.-P.; Huang, L.-B.; Roy, V. A. L. Functional High-*k* Nanocomposite Dielectrics for Flexible Transistors and Inverters with Excellent Mechanical Properties. *J. Mater. Chem.* **2012**, *22*, 14246−14253.

(21) Kim, S. K.; Han, S.; Jeon, W.; Yoon, J. H.; Han, J. H.; Lee, W.; Hwang, C. S. Impact of Bimetal Electrodes on Dielectric Properties of TiO_2 and Al-doped TiO_2 films. *ACS Appl. Mater. Interfaces* **2012**, *4*, 4726−4730.

(22) Yao, S.−H.; Dang, Z.−M.; Jiang, M.−J.; Bai, J. Grain Size Engineering for Ferroelectric $Hf_{0.5}Zr_{0.5}O_2$ Films by An Insertion of Al_2O_3 Interlayer. *Appl. Phys. Lett.* **2014**, *105*, 192903−1−5.

(23) Habazaki, H.; Koyama, S.; Aoki, Y.; Sakaguchi, N.; Nagata, S. Enhanced Capacitance of Composite Anodic ZrO_2 Films Comprising High Permittivity Oxide Nanocrystals and Highly Resistive Amorphous Oxide Matrix. *ACS Appl. Mater. Interfaces* **2011**, *3*, 2665−2670.

(24) Shaohui, L.; Jiwei, Z.; Jinwen, W.; Shuangxi, X.; Wenqin, W. Enhanced Energy Storage Density in Poly(vinylidene fluoride) Nanocomposites by a Small Loading of Suface-Hydroxylated $Ba_{0.6}Sr_{0.4}TiO_3$ Nanofibers. *ACS Appl. Mater. Interfaces* **2014**, *6*, 1533−1540.

(25) Dey, A.; De, S.; De, A.; De, S. K. Characterization and Dielectric Properties of Polyaniline−TiO_2 Nanocomposites. *Nanotechnology* **2004**, *15*, 1277−1283.

(26) Safenaz, M. R.; Al-Ghannam, S. M. Synthesis and Electrical Properties of Polyaniline Composite with Silver Nanoparticles. *Adv. Mater. Phys. Chem.* **2012**, *2*, 75−81.

(27) Virji, S.; Huang, J.; Weiller, B. H.; Kaner, R. B. Polyaniline Nanofiber Gas Sensors: Examination of Response Mechanisms. *Nano Lett.* **2004**, *4*, 491−496.

(28) Virji, S.; Kaner, R. B.; Weiller, B. H. Hydrogen Sensors Based on Conductivity Changes in Polyaniline Nanofibers. *J. Phys. Chem. B* **2006**, *110*, 22266−22270.

(29) Cho, S.; Kwon, O. S.; You, S. A.; Jang, J. Shape-Controlled Polyaniline Chemiresistors for High-Performance DMMP Sensors: Effect of Morphologies and Charge-Transport Properties. *J. Mater. Chem. A* **2013**, *1*, 5679−5688.

(30) Lee, K.; Cho, S.; Park, S. H.; Heeger, A. J.; Lee, C. W.; Lee, S. H. Metallic Transport in Polyaniline. *Nature* **2006**, *441*, 65−68.

(31) Cho, S.; Shin, K. H.; Jang, J. Enhanced Electrochemical Performance of Highly Porous Supercapacitor Electrodes Based on Solution Processed Polyaniline Thin Films. *ACS Appl. Mater. Interfaces* **2013**, *5*, 9186−9193.

(32) Kim, M.; Lee, C.; Jang, J. Fabrication of Highly Flexible, Scalable, and High-performance Supercapacitors Using Polyaniline/reduced graphene oxide Film With Enhanced Electrical Conductivity and Crystallinity. *Adv. Funct. Mater.* **2014**, *24*, 2489−2499.

(33) Kim, B.; Koncar, V.; Devaux, E.; Dufour, C.; Viallier, P. Electrical and Morphological Properties of PP and PET Conductive Polymer Fibers. *Synth. Met.* **2004**, *146*, 167−174.

(34) Yang, L.; Zhang, Z.; Wang, X.; Chen, J.; Li, H. In Situ Fourier-Transform Infrared Spectra Analysis of Hydrogen Bond in Polypropylene/Chlorinated Polypropylene/Polyaniline Composite. *Polym. Eng. Sci.* **2012**, *52*, 2627−2636.

(35) Yang, J.; Zhao, C.; Cui, D.; Hou, J.; Wan, M.; Xu, M. Polyaniline/Polypropylene Film Composites with High Electric Conductivity and Good Mechanical Properties. *J. Appl. Polym. Sci.* **1995**, *56*, 831−836.

(36) Yang, J.; Hou, J.; Zhu, W.; Xu, M.; Wan, M. Substituted Polyaniline-Polypropylene Film Composites: Preparation and Properties. *Synth. Met.* **1996**, *80*, 283−289.

(37) Valerio-Cardenas, C.; Romo-Uribe, A.; Cruz-Silva, R. Electrically Conducting Polypropylene/Polyaniline grafted-Short Glass Fiber Composites: Microstructure and Dynamic Mechanical Analysis. *Polym. Eng. Sci.* **2011**, *51*, 254−263.

(38) Imran, S. M.; Kim, Y. N.; Shao, G. N.; Hussain, M.; Cho, Y.-H.; Kim, H. T. Enhancement of Electroconductivity of Polyaniline/

DOI: 10.1021/acsami.5b05467
ACS Appl. Mater. Interfaces 2015, 7, 22301−22314

Graphene Oxide Nanocomposites Through In Situ Emulsion Polymerization. *J. Mater. Sci.* **2014**, *49*, 1328−1335.
(39) Potts, J. R.; Dreyer, D. R.; Bielawski, C. W.; Ruoff, R. S. Graphene-based Polymer Nanocomposites. *Polymer* **2011**, *52*, 5−25.
(40) Zheng, Q.; Xue, Q.; Yan, K.; Hao, L.; Li, Q.; Gao, X. Investigation of Molecular Interactions between SWNT and Polyethylene/Polypropylene/Polystyrene/Polyaniline Molecules. *J. Phys. Chem. C* **2007**, *111*, 4628−4635.
(41) Soroudi, A.; Skrifvars, M. Melt Blending of Carbon Nanotubes/Polyaniline/Polypropylene Compounds and Their Melt Spinning to Conductive Fibres. *Synth. Met.* **2010**, *160*, 1143−1147.
(42) Yang, L.; Chen, J.; Li, H.; Zhang, Z.; Wang, X. Synergistic Effect of Polyaniline and Multiwalled Carbon Nanotube on The Microstructure and The Electric Property in PP/PANI/MWNT Composites. *Polym. Eng. Sci.* **2012**, *52*, 979−987.
(43) Park, S.; An, J.; Piner, R. D.; Jung, I.; Yang, D.; Velamakanni, A.; Nguyen, S. T.; Ruoff, R. S. Aqueous Suspension and Characterization of Chemically Modified Graphene Sheets. *Chem. Mater.* **2008**, *20*, 6592−6594.
(44) Park, S.; An, J.; Jung, I.; Piner, R. D.; An, S. J.; Li, X.; Velamakanni, A.; Ruoff, R. S. Colloidal Suspensions of Highly Reduced Graphene Oxide in a Wide Variety of Organic Solvents. *Nano Lett.* **2009**, *9*, 1593−1597.
(45) Hong, J. Y.; Jang, J. Micropatterning of Graphene Sheets: Recent Advances in Techniques and Applications. *J. Mater. Chem.* **2012**, *22*, 8179−8191.
(46) Shin, K.-Y.; Hong, J.-Y.; Lee, S.; Jang, J. Evaluation of Anti-Scratch Properties of Graphene Oxide/Polypropylene Nanocomposites. *J. Mater. Chem.* **2012**, *22*, 7871−7879.
(47) Chang, D. W.; Lee, E. K.; Park, E. Y.; Yu, H.; Choi, H.-J.; Jeon, I.-Y.; Sohn, G.-J.; Shin, D.; Park, N.; Oh, J. H.; Dai, L.; Baek, J.-B. Nitrogen-Doped Graphene Nanoplatelets from Simple Solution Edge-Functionalization for *n*-Type Field-Effect Transistors. *J. Am. Chem. Soc.* **2013**, *135*, 8981−8988.
(48) Allen, M. J.; Tung, V. C.; Kaner, R. B. Honeycomb Carbon: A Review of Graphene. *Chem. Rev.* **2010**, *110*, 132−145.
(49) Al-Mashat, L.; Shin, K.; Kalantar-zadeh, K.; Plessis, J. D.; Han, S. H.; Kojima, R. W.; Kaner, R. B.; Li, D.; Gou, X.; Ippolito, S. J.; Wlodarski, W. Graphene/Polyaniline Nanocomposite for Hydrogen Sensing. *J. Phys. Chem. C* **2010**, *114*, 16168−16173.
(50) Cho, S.; Lee, J. S.; Jun, J.; Kim, S. G.; Jang, J. Fabrication of Water-Dispersible and Highly Conductive PSS-doped PANI/graphene Nanocomposites Using a High-Molecular Weight PSS Dopant and Their Application in H_2S detection. *Nanoscale* **2014**, *6*, 15181−15195.
(51) Shin, K.-Y.; Cho, S.; Jang, J. Graphene/polyaniline/poly(4-styrenesulfonate) Hybrid Film With Uniform Surface Resistance and Its Flexible Dipole Tag Antenna Application. *Small* **2013**, *9*, 3792−3798.
(52) Lee, J. S.; Kim, M.; Lee, C.; Cho, S.; Oh, J.; Jang, J. Platinum-Decorated Reduced Graphene Oxide/Polyaniline:poly (4-styrenesulfonate) Hybrid Paste for Flexible Dipole Tag-Antenna Applications. *Nanoscale* **2015**, *7*, 3668−3674.
(53) Wang, X.; Zhi, L.; Müllen, K. Transparent, Conductive Graphene Electrodes for Dye-Sensitized Solar Cells. *Nano Lett.* **2008**, *8*, 323−327.
(54) Hansen, C. M. *Hansen Solubility Parameters: A User's Handbook*, 2nd ed.; CRC Press: Hoboken, NJ, 2007.
(55) Maiti, P.; Nam, P. H.; Okamoto, M.; Hasegawa, N.; Usuki, A. Influence of Crystallization on Intercalation, Morphology, and Mechanical properties of Polypropylene/Clay Nanocomposites. *Macromolecules* **2002**, *35*, 2042−2049.
(56) Wang, N.; Gao, N.; Jiang, S.; Fang, Q.; Chen, E. Effect of Different structure MCM-41 Fillers With PP-g-MA on Mechanical and Crystallization Performances of Polypropylene. *Composites, Part B* **2011**, *42*, 1571−1577.
(57) Zhang, Q. X.; Yu, Z. Z.; Xie, X. L.; Mai, Y. W. Crystallization and Impact Energy of Polypropylene/$CaCO_3$ Nanocomposites with Nonionic Modifier. *Polymer* **2004**, *45*, 5985−5994.
(58) Nitta, K. H.; Asuka, K.; Liu, B.; Terano, M. The Effect of The Addition of Silica Particles on Linear Spherulite Growth Rate of Isotactic Polypropylene and Its Explanation by Lamellar Cluster Model. *Polymer* **2006**, *47*, 6457−6463.
(59) Causin, V.; Marega, C.; Marigo, A.; Ferrara, G.; Ferraro, A. Morphological and Structural Characterization of Polypropylene/Conductive Graphite Nanocomposites. *Eur. Polym. J.* **2006**, *42*, 3153−3161.
(60) Socrates, G. *Infrared and Raman Characteristic Group Frequencies: Tables and Charts*, 3rd ed.; Wiley-VCH: Weinheim, Germany, 1993.
(61) Su, S. J.; Kuramoto, N. Processable Polyaniline−Titanium Dioxide Nanocomposites: Effect of Titanium Dioxide on The Conductivity. *Synth. Met.* **2000**, *114*, 147−153.
(62) Salavagione, H. J.; Martínez, G.; Gómez, M. A. Synthesis of Poly(vinyl alcohol)/Reduced Graphite Oxide Nanocomposites With Improved Thermal and Electrical Properties. *J. Mater. Chem.* **2009**, *19*, 5027−5032.
(63) Hoffman, J. D.; Weeks, J. J. Melting Process and the Equilibrium Melting Temperature of Polychlorotrifluoroethylene. *J. Res. Natl. Bur. Stand., Sect. A* **1962**, *66*, 13−28.
(64) Skotheim, T. A.; Elsenbaumer, R. L.; Shacklette, L. W. *Handbook of Conducting polymers*, 2nd ed.; Marcel Dekker, Inc.: New York, 1997.
(65) He, F.; Lau, S.; Chan, H. L.; Fan, J. High Dielectric Permittivity and Low Percolation Threshold in Nanocomposites Based on Poly(vinylidene fluoride) and Exfoliated Graphite Nanoplates. *Adv. Mater.* **2009**, *21*, 710−715.
(66) Wang, Y.; Huang, S. W. Solution Intercalation and Relaxation Properties of Maleated Polypropylene/Organoclay Nanocomposites. *Polym.-Plast. Technol. Eng.* **2007**, *46*, 1039−1047.
(67) Xu, F.; Zhu, Y. Highly Conductive and Stretchable Silver Nanowire Conductors. *Adv. Mater.* **2012**, *24*, 5117−5122.
(68) Zheng, W.; Lu, X.; Wang, W.; Wang, Z.; Song, M.; Wang, Y.; Wang, C. Fabrication of Novel Ag Nanowires/Poly(vinylidene fluoride) Nanocomposite Film with High Dielectric Constant. *Phys. Status Solidi A* **2010**, *207*, 1870−1873.

DOI: 10.1021/acsami.5b05467
ACS Appl. Mater. Interfaces 2015, 7, 22301−22314